

# The Boreal Summer Madden–Julian Oscillation and Moist Convective Morphology over the Maritime Continent

BENJAMIN A. TOMS, SUSAN C. VAN DEN HEEVER, EMILY M. RILEY DELLARIPA,  
STEPHEN M. SALEEBY, AND ERIC D. MALONEY

*Department of Atmospheric Science, Colorado State University, Fort Collins, Colorado*

(Manuscript received 8 February 2019, in final form 23 September 2019)

## ABSTRACT

While the boreal summer Madden–Julian oscillation (MJO) is commonly defined as a planetary-scale disturbance, the convective elements that constitute its cloud dipole exhibit pronounced variability in their morphology. We therefore investigate the relationship between the intraseasonal cloud anomaly of the MJO and the convective elements that populate its interior by simulating a boreal summer MJO event over the Maritime Continent using a cloud-resolving model. A progressive relationship between convective cell morphology and the MJO within the convectively enhanced region of the MJO was identified and characterized as follows: anomalously long-lasting cells in the initial phases, followed by an increased number of cells in the intermediate phases, progressing into more expansive cells in the terminal phases. A progressive relationship does not seem to exist within the convectively suppressed region of the MJO within the simulated domain, however. Within the convectively enhanced region of the MJO, the progressive relationship is partially explained by the evolution of bulk atmospheric characteristics, such as instability and wind shear. Positive midlevel moisture anomalies coincide with anomalously long-lasting convective cells, which is hypothesized to further cascade into an increase in convective cell volume, although variability in the number of convective cells seems to be related to an unidentified variable. This intraseasonal relationship between convective cell morphology and the boreal summer MJO within the Maritime Continent may have broader implications for the large-scale structure and evolution of the MJO, related to both convective moistening and cloud-radiative feedbacks.

## 1. Introduction

Deep convective structures populate the tropics, provide the energetics that drive the large-scale tropical circulation, and interact with superimposed atmospheric waves (Riehl and Malkus 1957; Lorenz 1969; Hendon and Liebmann 1991; Kiladis and Weickmann 1992; Chang 1995; Lane et al. 2001; Fierro et al. 2009). The Madden–Julian oscillation (MJO; Madden and Julian 1971, 1972, 1994; Zhang 2005) is one such disturbance, and while the MJO is commonly defined according to its convective anomaly, its intraseasonal temporal scale and global spatial scale are substantially greater than that of typical mesoscale convective anomalies.

How important are mesoscale deep convective structures to the description of the MJO? Do mesoscale convective structures interact cross scale with the planetary-scale structure of the MJO? These questions have been topics of research for decades, and as computational and observational capabilities have improved over recent years, the ability to directly investigate them has similarly improved in tandem.

The MJO is an episodic disturbance within the equatorial tropics with a period of 30–80 days and can be defined by two distinct modes of variability, one during boreal summer and another during boreal wintertime (Madden 1986; Zhang and Dong 2004; Zhang 2005; Wu et al. 2006; Kikuchi et al. 2012). Historically, a plethora of research has focused on the characteristics of the wintertime form of the MJO or has considered the MJO to have consistent characteristics throughout the entire year (Hendon and Salby 1994; Wheeler and Hendon 2004). However, it has been shown that the consideration of the seasonality of the MJO is important both for developing real-time proxies for its location and

---

Supplemental information related to this paper is available at the Journals Online website: <https://doi.org/10.1175/JAS-D-19-0029.s1>.

---

*Corresponding author:* Benjamin A. Toms, [ben.toms@colostate.edu](mailto:ben.toms@colostate.edu)

DOI: 10.1175/JAS-D-19-0029.1

© 2020 American Meteorological Society. For information regarding reuse of this content and general copyright information, consult the [AMS Copyright Policy](#) ([www.ametsoc.org/PUBSReuseLicenses](http://www.ametsoc.org/PUBSReuseLicenses)).

magnitude and for process-based studies (Kikuchi et al. 2012; Kiladis et al. 2014; Jiang et al. 2018). Within this study, we focus on cross-scale interactions within the boreal summer MJO, which has been labeled with an assortment of identities, including the boreal summer intraseasonal oscillation (BSISO; e.g., Wang and Xie 1997; Kikuchi et al. 2012), summer MJO mode (Zhang and Dong 2004), or Indo-Pacific intraseasonal oscillation (Waliser et al. 2004).

While the MJO is commonly defined as a planetary-scale disturbance (Adames and Kim 2016), it is composed of a broad range of atmospheric phenomenon with scales ranging from individual convective cells (Riley et al. 2011; Zuluaga and Houze 2013; Barnes and Houze 2013; Riley Dellaripa et al. 2018) to expansive subtropical Rossby gyres (Kiladis et al. 2005). The convective mode of the MJO can itself be separated into various constituents. On the largest scale, a convective dipole exists, each pole of which can span thousands of kilometers longitudinally (Wheeler and Hendon 2004) (Fig. 1). The convective dipole gradually propagates eastward throughout the life cycle of the MJO, originating within the western Indian Ocean and decaying within the central Pacific Ocean. Within this dipole, synoptic convective anomalies generate and decay, sometimes taking the form of tropical cyclones (Maloney and Dickinson 2003; Li and Zhou 2013) or eastward-propagating inertia-Rossby waves (Yang and Ingersoll 2011) and Kelvin waves (Kikuchi et al. 2018). The mesoscales are also prominent (Barnes and Houze 2013; Vincent and Lane 2018; Riley Dellaripa et al. 2018), with convective elements ranging in scale from isolated convective elements to expansive mesoscale convective systems that generate their own subsynoptic circulations (Johnson and Kriete 1982; Hendon and Liebmann 1994). These convective elements meander within the planetary scale convective envelope, partially driven by the large-scale circulation and partially excited, maintained, and propagated by interactions with surrounding convective elements. In particular, the impact of vertical shear and convection-generated horizontal pressure gradients on mesoscale systems in the tropics can be of comparable magnitude to convective available potential energy (Moncrieff 2010). Such upscale effects of organized convection on the distribution of tropical precipitation and the intensity and multiscale structure of the MJO has been demonstrated by parameterizations of mesoscale convective systems implemented within both simple and complex climate models (Moncrieff et al. 2017; Yang et al. 2019). It is therefore apparent that mesoscale convective organization is important

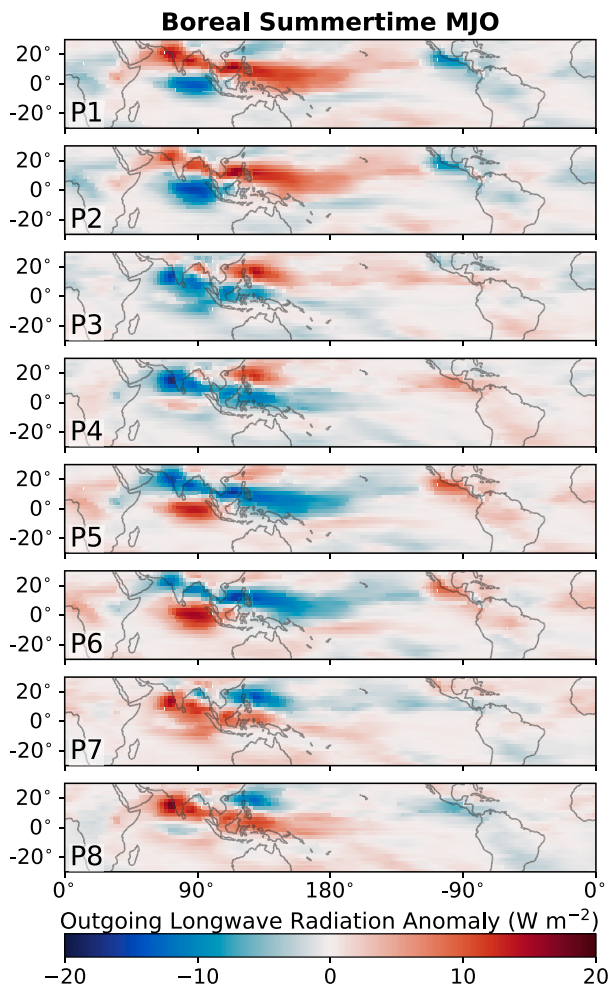


FIG. 1. Pentad OLR anomalies for the simulated MJO event based on OMI, reconstructed using the OMI principal components for each pentad. The anomalies shown are only for the 20–96-day anomalies represented by OMI and therefore do not directly consider the mesoscale convective structure of the MJO. Positive (negative) OLR anomalies correspond to suppressed (enhanced) convection.

for understanding the role of moist convection in climate in general, and particularly as it relates to the MJO.

When defined as a convective disturbance, the MJO is at its core an amalgamation of convective elements, each with its own lifespan and identifying characteristics. The life cycle of each MJO event can therefore possibly be described as a collection of convective features, which interact with each other and any local or upscale background environments they exist within. Tropical convection, within the MJO or otherwise, interacts with disturbances on larger scales than itself, although it is unclear to what extent convection acts as a conduit for upscale interactions (Mapes et al. 2006; Dias et al. 2012). Especially in vertically sheared environments, dynamical processes control the upscale

interaction of mesoscale convective systems (Lafore and Moncrieff 1989; Moncrieff 2010). We therefore ask, What information can be gleaned when such a bottom-up approach is taken to interrogating the structure of the MJO? *What insights can be made by equivalently considering both the mesoscale convective elements and the planetary-scale, intraseasonal convective anomalies?* In particular, we focus our attention on the Maritime Continent, wherein the evolution of the MJO is particularly complicated. We ask whether there exists a robust relationship between the mesoscale characteristics of convection within the core of the Maritime Continent and the intraseasonal structure of the MJO convective anomalies.

Cloud-resolving models (CRMs) offer the unique capability of capturing the cross-scale interactions within the MJO. By permitting the direct representation of cloud formation, the environments within which clouds form can be analyzed according to the governing physics of the atmosphere, rather than via convective parameterizations as is typically the case in global circulation models (Zhang and Mu 2005; Jiang et al. 2015; Moncrieff et al. 2012). We therefore simulate a boreal summer MJO event propagating over the Maritime Continent using a CRM to investigate whether any relationships exist between the mesoscales and intraseasonal-scale convective structures of the boreal summer MJO, in particular over the Maritime Continent. Within the simulation, the lateral boundaries are constrained with reanalysis, but mesoscale disturbances are permitted to freely develop within the interior of the domain. We then use spectral analysis to examine the low-frequency relationship between convective characteristics and the MJO, tying the relationship back to atmospheric state variables in a hypothesis for the relationship between convective morphology and the boreal summer MJO.

We first detail the CRM used to conduct the simulation along with characteristics of the simulated MJO event. The relationship between mesoscale convective morphology and the intraseasonal character of the MJO is then considered using both spectral analysis and phase compositing. Finally, we connect the relationship between the MJO and convective cell morphology across the Maritime Continent back to atmospheric state variables, and propose causal mechanisms for how intraseasonal anomalies in atmospheric thermodynamic and kinematic conditions relate to the convective structure of the MJO.

## 2. Simulation details

CRMs can directly represent the mesoscale characteristics of clouds without convective parameterizations, which permits an evaluation of how the state of the

atmosphere influences the development and evolution of cloud structures. The capability of CRMs to capture the evolution of cloud features on a structured four-dimensional  $(x, y, z, t)$  lattice is unique from that of observational data, which are typically inhomogeneous in resolution and sampling frequency. CRMs are therefore a powerful tool for evaluating the complete evolution of atmospheric systems across a broad range of scales, extending toward the smaller scales of atmospheric convection.

Of course, this capability is only of scientific interest if the model is representative of the real atmosphere and associated processes. While models should not necessarily be expected to identically reproduce the convective structure of the atmosphere given the chaotic nature of convection, a reliable model should produce statistics similar to observations. The Maritime Continent and tropics in general have few reliable mesoscale observational data such as surface observations and radar imagery, primarily due to the expansive oceans within the tropics. CRMs are therefore a critical tool for determining the structure of atmospheric phenomena within the tropics, and extend upon the more general information offered by satellite-based observations by also providing information regarding the underlying kinematic and thermodynamic state of the atmosphere.

We use the Regional Atmospheric Modeling System (RAMS; Cotton et al. 2003; Saleeby and van den Heever 2013), a CRM with a bin-emulating double-moment microphysics scheme, to simulate the entirety of a boreal summer MJO event. RAMS has previously been used to simulate the convective details of the boreal winter-time MJO, and it accurately captures the distribution of convective cell sizes compared to satellite observations, which further suggests it is a viable tool for simulating the convective identity of the MJO (Riley Dellaripa et al. 2018). Details of the simulation parameters are listed in Table 1, including the grid spacing, microphysical parameterizations, and lateral boundary conditions.

At the beginning of the simulation, the interior and lateral boundaries of the domain are initialized using ERA5 (Copernicus Climate Change Service 2017) and strongly nudged with a damping time scale of 30 min for the subsequent day. Thereafter, atmospheric state variables within the 20 grid cells closed to the lateral boundaries are nudged toward ERA5 data, while the interior of the domain is permitted to freely evolve according to the physics of the CRM (see Table 1 for additional details). This ensures that the synoptic-to regional-scale pattern of the MJO event is retained by ERA5 through the lateral boundary conditions, while the convective elements are permitted to form and

TABLE 1. Simulation parameters.

Model aspect	Setting
Model	Regional Atmospheric Modeling System (RAMS), version 6.2.07
Grid	Arakawa C grid $\Delta x = \Delta y = 4$ km; 3360-km longitudinal extent; 2920-km latitudinal extent $\Delta z$ varies with height Surface $\Delta z = 100$ m; domain top $\Delta z = 1000$ m Vertical stretch ratio = 1.10 42 vertical levels; model top: 25.5 km
Time integration	8-s time step 40-day simulation (8 Jul–17 Aug 2016) Output every 10 min
Initialization	ERA5 domain-wide initialization; 0.28 125° resolution (31 km at the equator) Central nudging with 4-h damping ( $\tau = 14\,400$ s) for first day of simulation Initial time: 0000 UTC 8 Jul 2016
Surface scheme	SST constrained by Reynolds SST observational dataset (Reynolds et al. 2002) Soil moisture nudged to ERA5 with 4-h damping Climatological NDVI representing continental vegetation
Boundary conditions	Open radiative lateral and upper boundaries (Klemp and Wilhelmson 1978) Lateral- and upper-boundary nudging to ERA5 with 30-min damping ( $\tau = 1800$ s) for entirety of simulation Lateral: 20 outermost grid cells along lateral boundaries Upper: From 20 km to upper boundary
Microphysics scheme	Two-moment bulk microphysics (Meyers et al. 1997) Eight hydrometeor classes (Saleeby and Cotton 2004)
Radiation scheme	Harrington (1997) two stream, updated every 30 min
Aerosol treatment	Aerosol species: Sulfates (Saleeby and van den Heever 2013) No aerosol sources or sinks Static (nonadvective) aerosol profile DeMott et al. (2010) ice nucleation parameterization
Turbulence scheme	Smagorinsky (1963) subgrid-scale closure

evolve freely. *The dominance of the CRM physics within the interior of the domain is critical to deriving conclusions relating convective morphology to the regional pattern of the MJO. The relative independence of the formation of clouds from the lateral boundary conditions permits the simulation to directly capture the evolution of atmospheric physics on scales ranging from multiple kilometers to hundreds of kilometers.* We can therefore analyze how the convective scales of the atmosphere interact with the regional-scale anomalies associated with the MJO.

#### a. MJO event details

The MJO event was identified using the outgoing longwave radiation MJO index (OMI; Kiladis et al. (2014)), which explicitly considers the seasonality of the MJO and therefore captures the defining structures of the boreal summer MJO (as was shown in Fig. 1). OMI is derived using principal component analysis of eastward-only anomalies in outgoing longwave radiation (OLR) with periods of 30–96 days, which is then projected back onto a 20–96-day basis that includes both eastward- and westward-propagating waves. Since OLR is a proxy for high clouds given that they emit at

lower temperatures, OMI is a proxy for the regional, low-frequency cloud identity of the MJO [see Liebmann and Smith (1996) for a description of how OLR is calculated]. The entirety of the July–August 2016 MJO event was simulated from inception to demise, which maintained at least a one standard deviation OMI principal component magnitude convective anomaly from 8 July through 17 August and throughout all eight phases of the OMI phase space (Fig. 2). The convective anomaly originated within the Indian Ocean and progressively propagated northward and eastward across the Maritime Continent and South China Sea. Within visible satellite imagery, it is apparent that a diverse collection of convective features formed within the convective dipole, including diurnally forced continental convection, maritime mesoscale convective systems, and even a tropical cyclone on the fringe of the Philippines archipelago (images not shown).

#### b. Simulation domain

The simulation domain is centered over the Maritime Continent and South China Sea (Fig. 3), over which the convective dipole of the boreal summer MJO

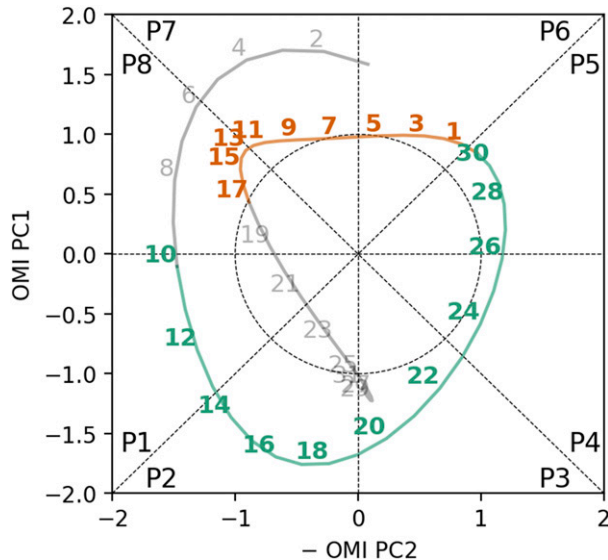


FIG. 2. OMI principal component phase space for the July–August 2016 boreal summer MJO event. Dates that were analyzed are colored, while dates outside of the analyzed simulation data are gray. July dates are green and August dates are orange. Note that the principal component ordering has been changed to ensure this phase-space diagram can be compared directly to the conventional real-time multivariate MJO index phase-space diagram as originally developed in Wheeler and Hendon (2004).

propagates. The orography within the domain is coarsened to the 4-km simulation grid, where the orography of each grid point is the average of native 30-arc-s ( $\sim 1$ -km) orographic data. During phase 1 of the simulated MJO event, a majority of the simulation domain is within the suppressed lobe of the convective dipole (Fig. 4). As the MJO progresses throughout its phase space, the convectively enhanced lobe propagates north and east throughout the domain and is gradually replaced by the suppressed lobe, such that the entirety of the domain is influenced by the convectively enhanced and suppressed regions of the dipole for at least some time throughout the evolution of the MJO.

Computing limitations prevent us from employing a domain that spans both the Indian Ocean and west Pacific and we acknowledge this as a caveat. We acknowledge that Indian Ocean oceanic precipitation might have different organization than represented here. However, we feel that our domain is well suited for analyzing the complete life cycle of a northward-propagating ISO event in the MC and west Pacific since it captures the initiation of northward propagation near the equator and its demise at the northern edge of the domain. Our analysis of cloud morphology is thus highly relevant to understanding the initial stages of northward-propagating BSISO disturbances,

the maintenance of BSISO convective anomalies through the region of strong northward propagation, and the reasons for demise of BSISO convection on the north side of the domain.

### 3. Comparison between the simulation and observations

As previously discussed, the unique capability of CRMs to capture the higher-frequency, or mesoscale, evolution of the atmosphere is only scientifically viable if the model reproduces the low-order statistics available from observations. We therefore compare the simulation to ERA5 and satellite observations to ensure the simulated large-scale structure of precipitation and atmospheric state variables such as temperature and wind are similar to observationally based analyses.

The regional characteristics of the MJO event, such as zonal wind and precipitation anomalies, are captured well by the simulation (Figs. 5 and 6); 850-hPa zonal wind anomalies (U850) are compared between the simulation and ERA5 at the locations marked by the red dots in Fig. 3, which were chosen to compare locations both nearby and distant from the lateral boundaries of the simulation domain (Fig. 5). As should be the case, U850 anomalies deviate most substantially from ERA5 in the interior of the domain, where the lateral boundary conditions have the least influence and where the influence of mesoscale and synoptic-scale contributions to the zonal wind are captured by the CRM (Fig. 5). The intraseasonal (i.e.,  $>20$ -day periodicity) U850 variability within the simulation aligns well with reanalysis, although the simulation exhibits a slightly dampened amplitude within the interior of the domain. The higher-frequency variability of the simulation with periods of less than 20 days deviates more substantially from that of ERA5, which is also to be expected given that we have designed the simulation to permit the free evolution of meso- and synoptic-scale disturbances within the interior of the domain. The capability of the simulation to capture this higher-frequency variability, in particular that within the mesoscales, offers an opportunity to generate statistics for and deduce mechanisms driving the higher-frequency modes associated with the MJO that are not directly captured by the reanalysis.

Observational precipitation data from the Global Precipitation Measurement (GPM; Hou et al. 2014) mission Integrated Multisatellite Retrievals for GPM (IMERG; Huffman et al. 2015) product depict intraseasonal anomalies in precipitation propagating northward and eastward

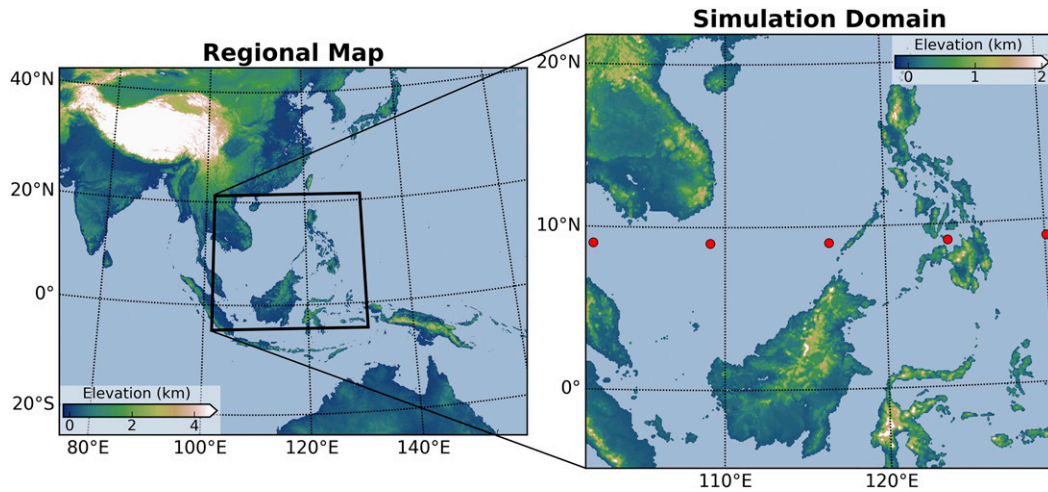


FIG. 3. (left) Topographic map of the Indo-Pacific region, with the simulation domain outlined in black. (right) Topographic map of the simulation domain. The red dots denote the locations where data were extracted for the comparison between RAMS and ERA5 in Fig. 5. Note that the color scales are different between the regional map and the simulation domain. Topography is not extracted from the model, but rather shows the topography at 30-s resolution (approximately 100 m at the equator).

across the domain throughout the simulation period (Fig. 6a). The northward-propagating mode is more well pronounced than the eastward-propagating mode, progressing from the southern through northern extents of the domain throughout the simulation period. The northward-propagating characteristics are captured

well by the simulation, while relatively more differences exist between the observed and simulated eastward-propagating intraseasonal component (Fig. 6b). The spatiotemporal bounds of the intraseasonal precipitation anomalies with greater than 20-day periodicity align well between the observations and simulation,

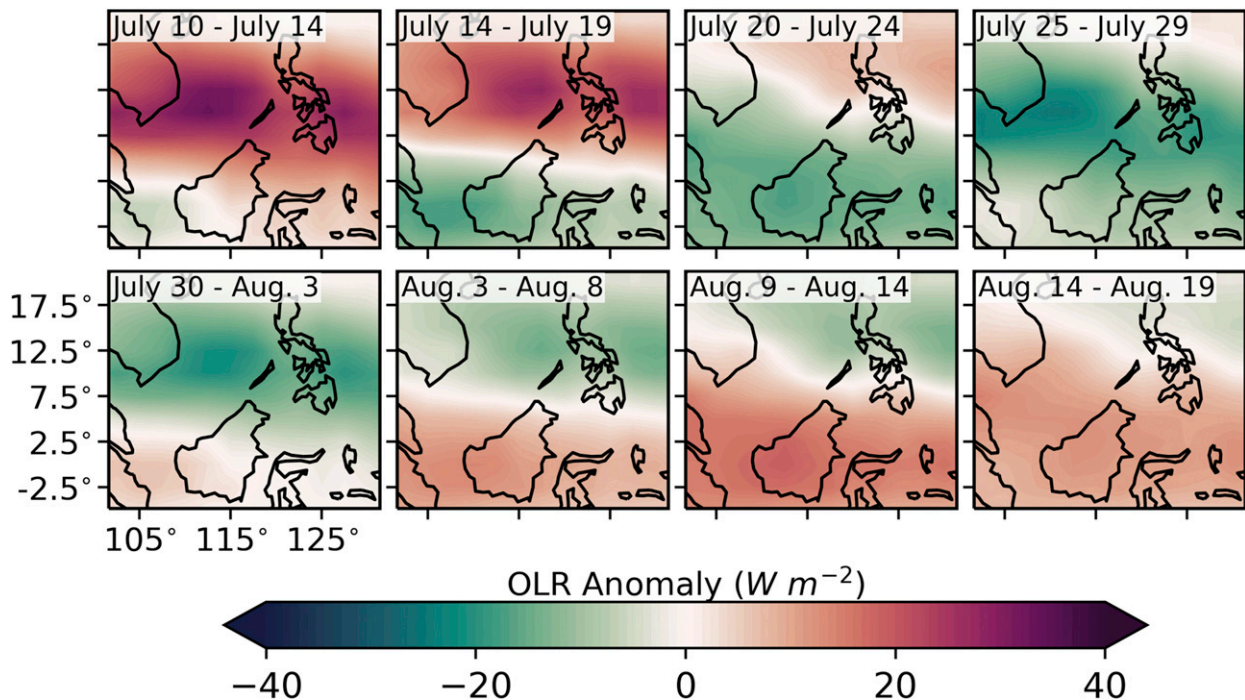


FIG. 4. OLR anomalies for each phase of the boreal summer MJO. Anomalies correspond to a  $1\sigma$  MJO event using the OMI EOF patterns for 31 Jul. Green (red) denotes negative (positive) OLR anomalies, which signifies enhanced (suppressed) convection.

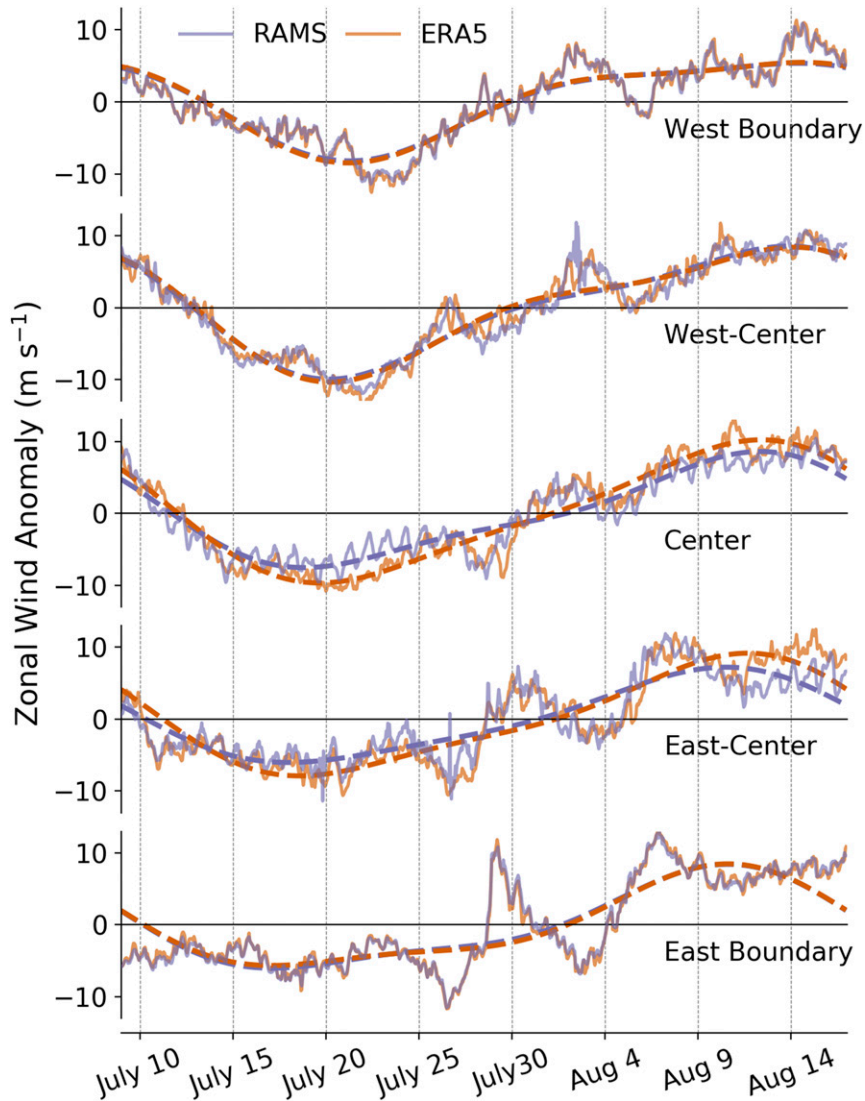


FIG. 5. Time series of 850-hPa zonal wind anomalies for the RAMS simulation and ERA5 across the simulation domain, as labeled by the red dots in Fig. 3. The solid lines show the unfiltered time series while the dashed lines show only the >20-day variability.

particularly for the northward-propagating mode (Figs. 6c,d). Perhaps the most notable difference between the simulation and observations is the tendency for the simulation to not capture the full westward extend of intraseasonal anomalies from the Filipino archipelago (longitudes west of  $120^\circ$ ). While westward propagation of convection does occur within the simulation, it is apparent from Fig. 6f that the westward propagation is not as prominent within the simulation as in observations. It is worth noting that the simulation captures the predominant eastward-propagating signal during the 15 July through 5 August period, after which the intraseasonal anomalies appear to revert

back westward toward the Filipino archipelago. Another prominent difference between the simulation and observations is the tendency for the simulation to have more intense precipitation over land. It is unclear why this discrepancy exists, although it may relate to the usage of static aerosol profiles and the dependence of rainfall generation within cloud microphysics schemes on aerosol concentrations (Saleeby and van den Heever 2013).

The simulation accurately captures the evolution of the MJO event from a regional perspective based on the similarities between the simulated and observed intraseasonal structure of zonal winds and precipitation throughout the simulation period.

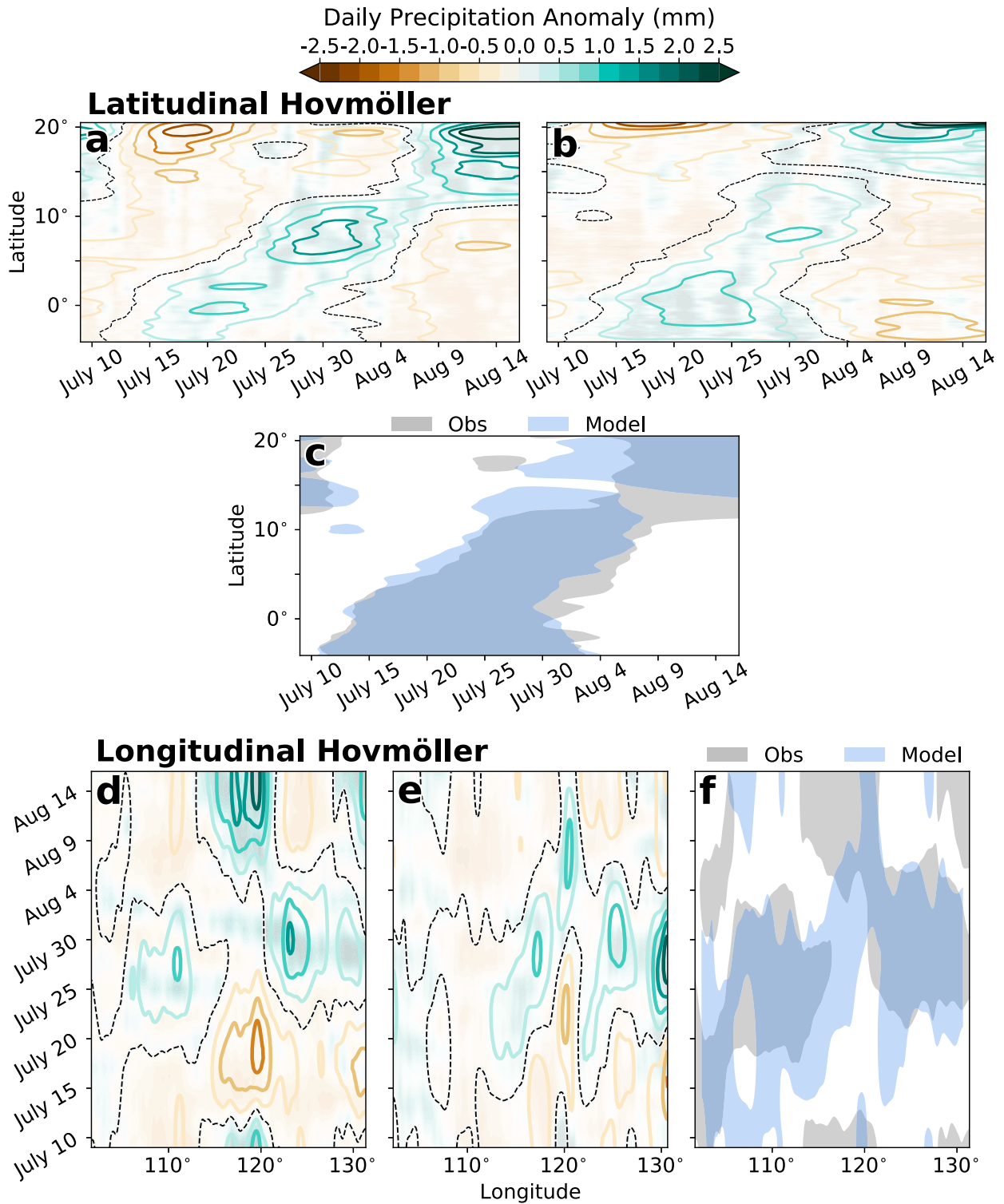


FIG. 6. (a) Latitudinal Hovmöller diagrams of precipitation anomalies from the domain-wide, simulation-long mean from GPM observations. The total precipitation anomalies are filled, while the open contours show the intraseasonal ( $>20$  days) anomalies. (b) As in (a), but for the simulated precipitation using the RAMS CRM. (c) Comparison between observations (gray) and the simulation (blue) of the locations of intraseasonal precipitation anomalies, where positive anomalies are shaded and negative anomalies are unshaded. (d)–(f) As in (a)–(c), but for the longitudinal Hovmöller diagrams.

We therefore use the CRM simulation to analyze the convective structure and mesoscale processes of the MJO event.

#### 4. Convective tracking algorithm

We utilize a convective cloud tracking algorithm to generate a database of convective events that occur throughout the simulation. The algorithm is based on thresholds of cloud condensate, precipitation rates, and the fraction of grid cells associated with one convective feature that overlaps other convective cells in sequential time steps. Briefly, the logic of the algorithm is as follows:

- 1)  $T = 0$ : Identify all contiguous regions of cloud (i.e., cloud mass mixing ratio greater than  $1 \text{ g kg}^{-1}$ ) with a volume of at least  $50 \text{ km}^3$  that are also associated with at least one point with a surface precipitation rate greater than  $5 \text{ mm h}^{-1}$  within the extent of their cloudy region.
- 2)  $T = 0 + \Delta t$ : Identify all contiguous regions of cloud (i.e., cloud condensate greater than  $1 \text{ g kg}^{-1}$ ) with a volume of at least  $50 \text{ km}^3$  that are also associated with at least one point with a surface precipitation rate greater than  $5 \text{ mm h}^{-1}$  within the extent of their cloudy region.
- 3) Link the convective cloud elements identified in steps 1 and 2 by considering clouds that overlap with a fraction greater than 0.75 to be the same convective element evolved across time.
- 4) Repeat steps 2 and 3 for the remainder of the simulation.

The tracking algorithm is not particularly sensitive to the selected thresholds if values  $\pm 25\%$  of those presented in this paper are used; the qualitative conclusions we draw at the end of the paper are therefore independent of the selection of the threshold values. It is important to note that since all identified cloud objects must be associated with a minimum precipitation threshold that is representative of convective cells (Petersen and Rutledge 2001), the subsequent analysis only considers actively precipitating convective clouds and purposely neglects other cloud features, such as nonprecipitating cumulus, residual glaciated clouds, and other general types of nonprecipitating clouds. Given the different microphysical and thermodynamic processes governing the evolution of convective and stratiform precipitation (Houze 1997), we focus on the convective aspects of the MJO, although completing an analysis for solely stratiform precipitation would be a worthwhile endeavor as well.

An example convective cloud structure identified by the algorithm is shown in Fig. 7. Within this particular case, multiple cell mergers ( $t = 1$  and  $2 \text{ h}$ ) and splits ( $t = 4$  and  $5 \text{ h}$ ) can be observed, along with a shallow arcing band of cloud that is likely associated with the cold pool of the convective cell ( $t = 7$  and  $8 \text{ h}$ ). In the case of a cell split, a new cell label is created for the cell that least overlaps with the cell structure from the previous time step, while the other cell that most overlaps with the original cell maintains the original label. Based on a clustering of cloud features identified by the convective cloud feature tracking algorithm, the algorithm captures convective structures with a broad range of spatial and temporal characteristics, ranging from isolated, transient convective cells to expansive, persistent mesoscale convective systems (clustering data not shown). In total, 180 000 convective elements were identified within the simulation.

Figure 8 shows the cloud tracks for each convective cell identified within the simulation, along with the maximum size each convective cell achieved. Of note, the algorithm only tracks convective features that are at least  $100 \text{ km}$  away from the lateral boundary of the domain to limit any potential contamination caused by the lateral boundary nudging. The spatial pattern of convective tracks produced by the simulation is similar to the July and August precipitation climatology of the region (Biasutti et al. 2012).

Two pronounced regions of convective minima exist: one within the north-central South China Sea and the other between the southern tip of the Philippines and Borneo. The minimum within the South China Sea is associated with a rain shadow induced by winds flowing down the slope of the elevated topography on the eastern coast of Indochina (Wang 2002; Xu et al. 2008). Numerous convective maxima are also present, the most pronounced of which are atop eastern Indochina, west of the Philippines archipelago within the eastern fringes of the South China Sea, east of the Philippines archipelago within the Philippines Sea, atop Borneo, and along the southern fringes of the South China Sea. The maximum west of the Philippines archipelago is associated with the offshore propagation of diurnally driven convection (Love et al. 2011), while the convectively active region over eastern Indochina is similarly associated with both a persistent diurnal cycle and monsoonal flow within the broader Southeast Asian monsoon (Zhang et al. 2002). Within the Philippine sea, easterly waves propagating toward the Maritime Continent excite convection of various modes including two tropical cyclones (not shown), while the banding structure

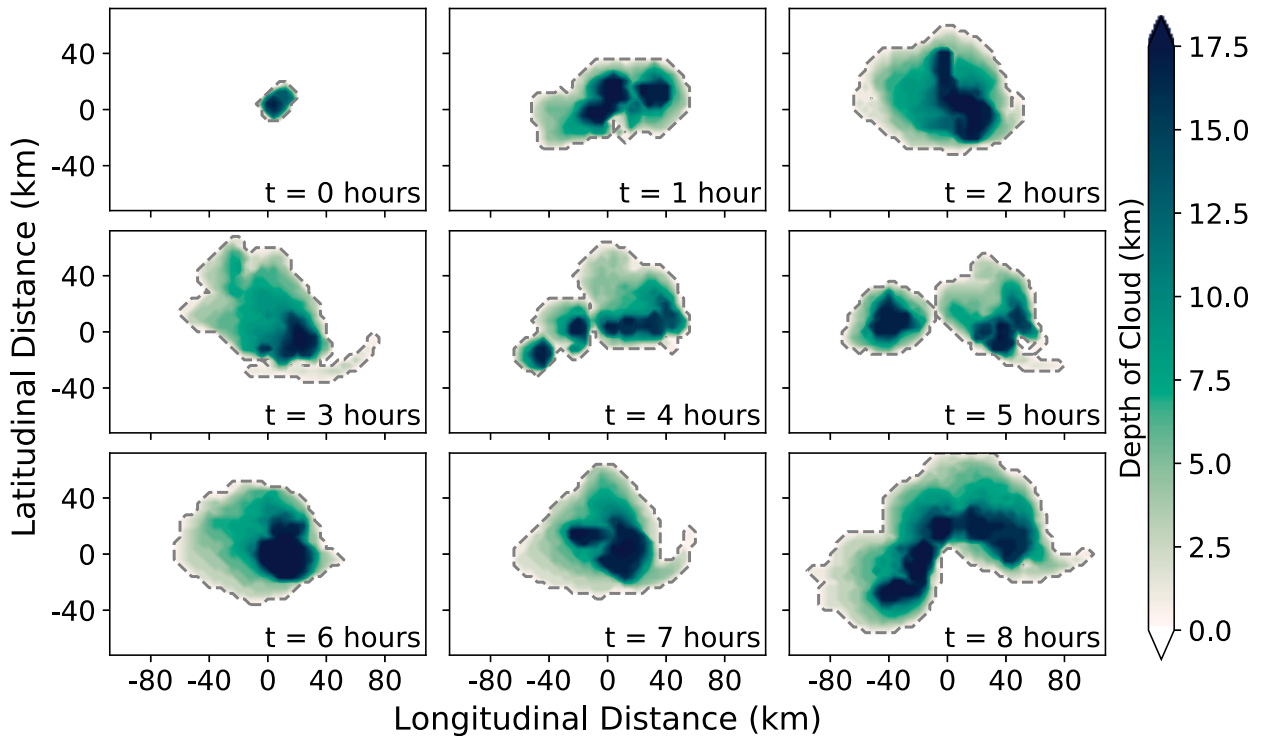


FIG. 7. Example convective cell that was identified and tracked by the convective cell tracking algorithm developed for this research. Each frame depicts an hour of convective evolution. The convective cell is centered about its centroid for each time for the purposes of this visualization, although it is not stationary within the simulation. The lateral extent of the cloud is demarcated by the gray dashed line.

along the southern periphery of the South China Sea results from a tail of convection that forms on the southwest side of the aforementioned tropical cyclones. While tropical cyclones can be thought of as distinct entities from the MJO, they can both modulate and be modulated by intraseasonal variability, and

are therefore an important constituent of the overall convective morphology of the MJO (e.g., Hsu et al. 2008; Kikuchi and Wang 2010; Li and Zhou 2013). In summary, the simulation accurately captures the climatological convective response of the Maritime Continent, and therefore provides alucrative opportunity for

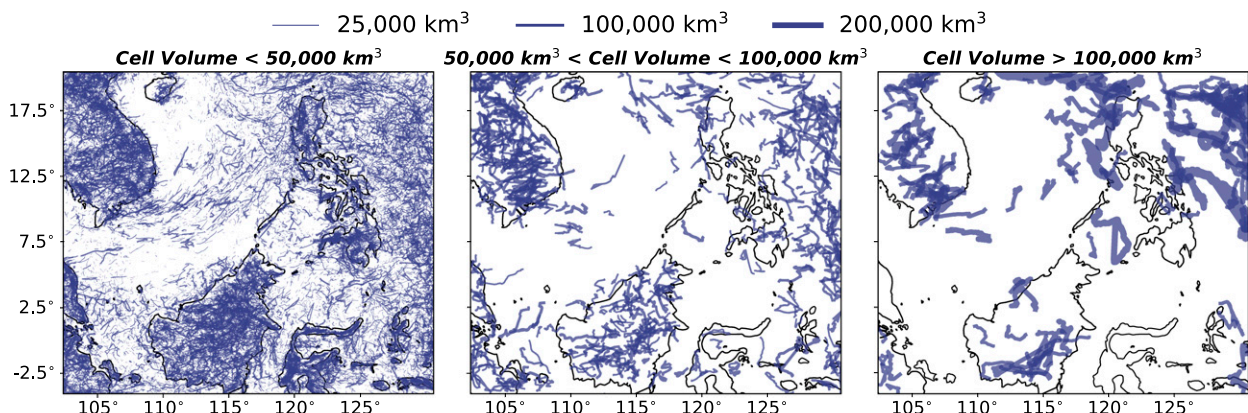


FIG. 8. Tracks for all convective events identified within the simulation, showing the centroids of the convective cells at 10-min intervals. The width of the tracks signifies the maximum volume of the respective convective cell throughout its lifetime: (left) volumes less than  $50\,000 \text{ km}^3$ , (center) volumes greater than  $50\,000 \text{ km}^3$  and less than  $100\,000 \text{ km}^3$ , and (right) volumes greater than  $100\,000 \text{ km}^3$ . A total of approximately 180 000 tracks are plotted.

investigating the modulation of the background convective morphology by the MJO.

## 5. Low-frequency convective evolution

We now analyze the relationship between the boreal summer MJO and convective cell longevity, volume, and cell number using two methods. For the first method, Fourier-based spectral filtering of time series of the median values of these three cell characteristics is used to explicitly remove any patterns not directly associated with the intraseasonal time scales of the MJO. The results of the spectral filtering are then corroborated by compositing unfiltered time series of the convective characteristics into two-dimensional histograms according to MJO phase.

We take care to not distinctly separate the impacts of geography on intraseasonal variability from the analysis. By not removing the impacts of geography on the intraseasonal time scales, we capture the relationship between mesoscale convection and the intraseasonal structure of the MJO as it exists in an Earth system with complex geography. It would be interesting to remove the impacts of geography through either statistical methods or by removing orography from the simulation domain, although that is not our intention for this study. It is worth noting that we do remove some aspects of geographical variability by filtering for intraseasonal time scales, such as the removal of the diurnal cycle.

### *a. Frequency-based analysis*

For the frequency-based analysis, we generated time series of convective characteristics for the enhanced and suppressed regional convective anomalies of the MJO prior to spectral filtering. For example, for the enhanced convective anomaly, we identified the regions of negative OLR anomalies associated with the MJO based on the daily principal component time series of the observational OMI. The regions of the negative (convectively enhanced) and positive (convectively suppressed) OLR anomalies associated with the MJO may generally be inferred from Fig. 4, although Fig. 4 shows the pentad-averaged OLR anomalies and this analysis considers daily OLR anomalies. We then calculated the number of cells, median convective cell longevity, and median volume for each 10-min period of the simulation. We use the median rather than the mean since the median does not assume a Gaussian distribution, and is therefore a more generalizable statistic. The median convective cell longevity for each 10-min period was calculated by finding the median longevity of all cells that existed during that 10-min period, including their lifespan

before and after the specified 10-min period. This generated a single time series for each of the three variables for the convectively enhanced portion of the MJO's convective dipole. The mean was then removed from each time series to generate anomalous time series for each variable. These anomalous time series were then spectrally decomposed using a Fourier transform, and harmonics with periods of less than 20 days were removed. The predominant signal within the  $\geq 20$ -day periods are those associated with the MJO since the summertime MJO accounts for approximately 60% of intraseasonal ( $>20$  days) convective variability within the tropics (Kiladis et al. 2014). We followed this process for both the convectively enhanced and suppressed regions of the MJO.

Figure 9 presents the relationship between convective characteristics and the intraseasonal scales of the boreal summer MJO, separately for the convectively enhanced and suppressed regions. These figures are presented in radial space, analogous to the phase spaces used to represent the principal component phase space of the MJO (Wheeler and Hendon 2004; Kiladis et al. 2014). Since we intentionally selected an MJO event that is representative of canonical MJO events, the structure of these figures likely represents a progressive evolution that may be identified within other canonical MJO events.

Within the convectively active lobe, the relationship between the boreal summer MJO and convective organization proceeds sequentially as follows: increased cell longevity in the initial phases, followed by increased cell number in the intermediate phases, progressing into increased cell volume in the terminal phases (Fig. 9a). The relationship is progressive, whereby one pattern gradually blends into the next, with the maxima of the oscillations in each convective characteristic being separated by approximately  $120^\circ$  within the phase space. The convective characteristics within the convectively active region of the MJO can therefore be distinctly separated into three distinct regimes. In the first regime during phases 1 and 2, convective cells gradually decrease in size, last longer, and are fewer in number. The second regime occurs from phase 3 through the earlier portions of phase 6, wherein more convective cells exist, but the cells are anomalously small in volume. The third regime occurs during the latter portions of phase 6 through the demise of the MJO event, and is characterized by anomalously expansive convective cells, but a lesser number of unique convective features and gradually increasing cell longevity. It is worth noting that the number of cells within the convectively active region (green line in Fig. 9a) does not scale directly with the area of the simulation domain within the convectively

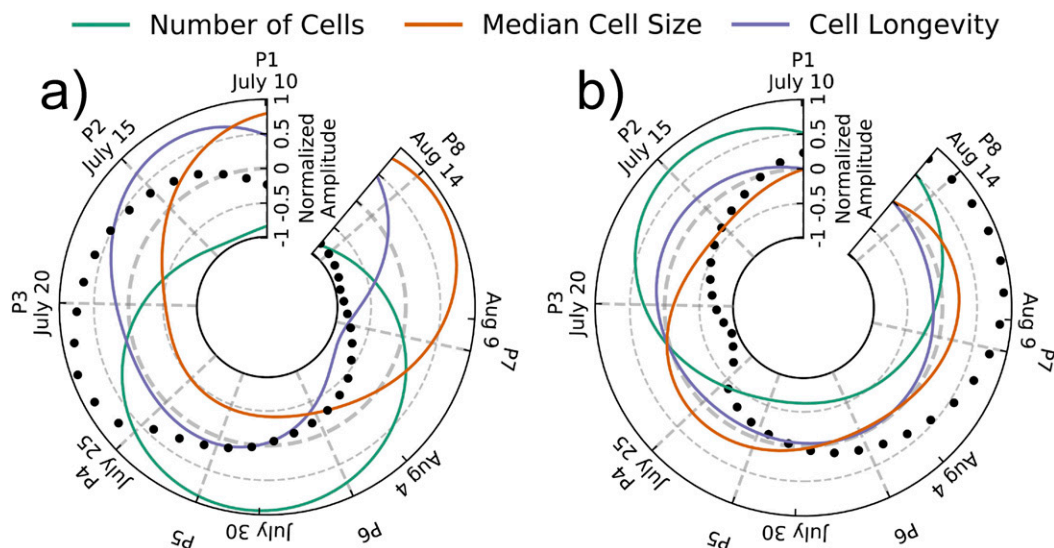


FIG. 9. Radial time series of low-frequency ( $>20$  days) variability in the number of convective cells (green), cell volume (orange), and cell longevity (purple) for the (a) convectively enhanced region and (b) convectively suppressed region of the MJO, as defined by OMI. The black dots denote the fraction of the domain within the convectively enhanced region, with a normalized amplitude of  $-1$  corresponding to 0% of the domain and a normalized amplitude of 1 corresponding to the entire domain. The following normalization factors were used to plot all variables on the same y axis: cell number, 150; cell volume,  $6000 \text{ km}^3$ ; and cell longevity, 60 min.

active region (black dots in Fig. 9a), which implies that a relationship between convective cell number and the MJO does exist beyond a simple change in the area being sampled as the MJO OLR anomalies traverse the domain.

The consideration of this intraseasonal relationship in the context of all frequencies of convective variability is important for justifying its importance for the overall convective evolution within the tropics. Intraseasonal anomalies in cell number account for 22.8%, size for 7.8%, and longevity for 17.3% of all variability with periodicities less than or equal to 40 days, which was the duration of the simulated MJO event. These percentages represent a lower bound of the impacts of intraseasonal variability on convective characteristics, as the intraseasonal modes of variability may also impact higher-frequency modes of variability (e.g., the diurnal cycle and synoptic modes such as tropical cyclones).

Convective cell morphology exhibits a less pronounced progressive relationship within the convectively suppressed regime (Fig. 9b). Generally, only small anomalies in convective cell size and longevity occur within the suppressed lobe, although the number of cells is increased during phases 1 and 2, and again in phase 8. This relative lack of a cycle can be interpreted as the convectively suppressed regimes maintaining their mean-state characteristics regardless of MJO

phase. Additionally, the differences between the convectively enhanced and suppressed regions suggests that the cycle observed within the convectively enhanced regions is not entirely related to geographical changes as the MJO traverses the Maritime Continent. If the cycle were caused by geographical changes, then both the active and suppressed convective regimes would exhibit a similar but phase-shifted cycle, which is not the case.

#### b. Phase composites

For the compositing-based analysis, we considered convective anomalies of all frequencies but still separately considered the convectively enhanced and suppressed regions of the MJO. That is, we use the unfiltered time series of convective characteristics that have only had their mean removed, which were constructed as discussed in the previous section.

The following procedure describes how two-dimensional histograms were constructed for both the convectively active and suppressed regimes. We first identified all convective features that occurred within the convectively enhanced regime for each respective phase, as defined by OMI. Two-dimensional histograms comparing each combination of convective characteristic were then generated for each phase. We also calculated the two-dimensional histograms for all convective features within the convectively enhanced

region, regardless of MJO phase, which rendered a singular two-dimensional histogram for the entire MJO event for the convectively enhanced regime. Both the phase-specific histograms and the histogram for the entire MJO event were normalized by the sum of their respective bins. The anomalous characteristics for each phase were then calculated by dividing the normalized, phase-specific histograms by the normalized histogram for the entire MJO event. These anomalous histograms represent the fractional difference between the convective characteristics of each individual phase and the overall MJO event. The anomalous histograms were then plotted on a logarithmic scale with base 10, and show fractional differences from the background state for each phase, with negative values denoting a reduction in convective features for a bin and positive values denoting an increase.

The phase-composited two-dimensional histograms corroborate the results presented within the frequency-based analysis. The similarities between the phase-composited histograms and the spectral analysis suggests that the relationship within the spectrally filtered time series is not disrupted by higher-frequency modes of variability. Particularly, this relative lack of importance of the higher-frequency modes suggests that if geographic variability is important to the relationship between mesoscale convection and the intraseasonal time scales of the MJO, the importance is well captured by the intraseasonal relationship. The two-dimensional histograms for the cell longevity and cell expanse are in the online supplemental material since the information is redundant with the previous section, although we present the two-dimensional histogram between convective cell depth and cell volume to provide an additional perspective on the convective morphology (Figs. 10 and 11). Within the convectively enhanced region of the MJO, the frequency-based analysis in section 5a suggested that convective cells are most expansive during the latter phases of the MJO, namely phases 7 and 8. Figure 10 corroborates this pattern, with the most expansive convective cells occurring during phases 7 and 8, as seen by the large positive fractional difference values along the right edge of the colored bins. The expansiveness of the shallow convective mode that extends to the middle troposphere also increases during the latter phases, as seen by the increased number of convective clouds between 5 and 12 km deep during phases 7 and 8.

Within the convectively suppressed region of the MJO, the relationship between convective cell depth is opposite to that of the convective enhanced region (Fig. 11). Specifically, the deepest convective cells occur

during the intermediate phases of the MJO, whereas relatively shallower convective cells exist during the early and late phases. Unlike the convectively enhanced region, however, the anomalous convective depth and longevity is not bimodal during the phases characterized by the deepest convection. The convectively suppressed regime is located across the northern South China Sea and Philippines archipelago during the intermediate phases, similar to the location of the convectively enhanced regime during the later phases of the MJO. This similar, phase-shifted relationship between the enhanced and suppressed phases of the MJO suggests that convective depth may be tied to geographical variability within the Maritime Continent, which does not seem to be the case for cell longevity, expanse, or number.

## 6. Convection evolution and the atmospheric state

We investigate the low-frequency evolution of the atmospheric state within the simulation in an attempt to physically explain the relationship derived in section 5a. The relationship between mesoscale convective morphology and the intraseasonal time scales of the MJO is much less apparent within the convectively suppressed regions than within the convectively enhanced regions, based on both the spectral analysis and phase composites of section 5. So, within this section we only investigate the low-frequency evolution of the atmospheric state within the convectively enhanced region in an attempt to explain how the large-scale environment may be tied to the mesoscale–intraseasonal relationship. The intraseasonal evolution of the atmospheric state is defined similarly to the rest of the paper, and we only consider anomalies with periods of greater than 20 days, which are isolated using a bandpass spectral filter. Furthermore, only the atmospheric state at convective initiation is considered since the convective life cycle is much shorter than the periods of atmospheric anomalies being considered within the spectrally filtered time series ( $\sim 6$  h for persistent convective systems compared to  $>20$  days for the atmospheric anomalies). The atmospheric state at convective initiation is therefore most representative of the atmospheric state throughout the entire convective life cycle, although convection does feedback upon its environment, so the atmospheric state would still likely change throughout the convective life cycle. The location of convective initiation is defined as the  $(x, y)$  centroid of the convective cells at the first time step they were identified. Since we define the atmospheric state for each convective cell according to the location of convective initiation, we also separate the subsequent analysis by convective events

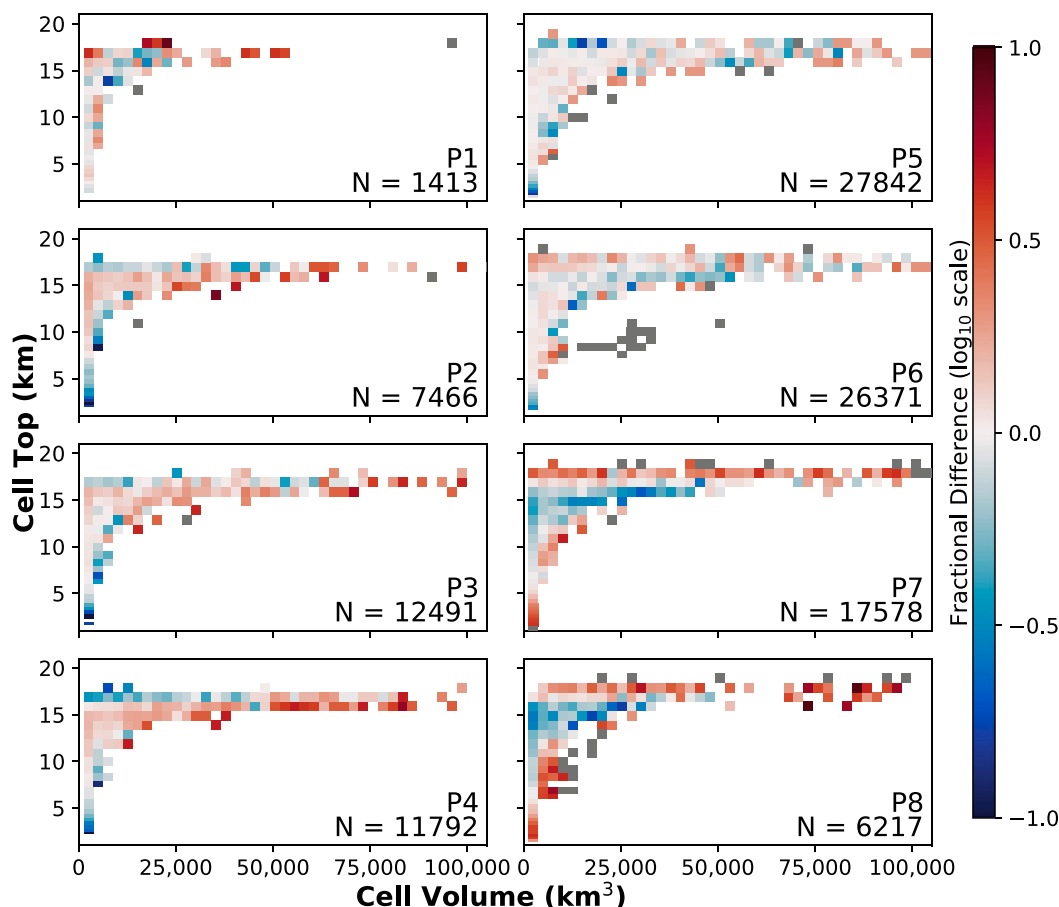


FIG. 10. Two-dimensional histograms of cell top ( $y$  axis) and cell volume ( $x$  axis) for convectively enhanced regions during each phase of the MJO. Regions that are included within the convectively enhanced portion of the MJO are defined as regions with negative OLR anomalies, as shown in Fig. 4. The histograms show the anomalous fractional occurrence for each bin relative to the histogram for the entire domain and entire simulation. Red regions denote an increase in occurrences in the respective phase relative to the simulation mean, while blue regions denote a relative decrease. Gray patches indicate regions where all cases are attributed to a single phase. The number of convective cells included in each phase is listed in the bottom-right corner of each histogram.

that occur within the convectively enhanced and suppressed regions of the MJO, similar to the analysis presented in section 5.

The connection between convective cell morphology and intraseasonal variability in the atmospheric state was considered using the bulk parameters of vertical wind shear, convective available potential energy (CAPE), and convective inhibition (CIN). We calculated the low-frequency evolution of these bulk parameters according to the following method. First, low-frequency anomalies in atmospheric state variables such as temperature, water vapor mixing ratio, and zonal and meridional wind were calculated. These low-frequency anomalies were calculated for each grid cell within the  $(x, y, z)$  space. The anomalous time series for each variable were calculated by removing

the simulation mean value for each grid cell. A band-pass filter was then applied that removes anomalies with periods of less than 20 days, which resulted in low-frequency time series with intraseasonal anomalies with periods of greater than 20 days. It is important to note that these anomalies represent anomalies from the mean state of the simulation. Since the simulation included the full cycle of an MJO event from its enhanced to suppressed phases, these anomalies are thereby also anomalies from the background state.

We filter the atmospheric state variables in  $(x, y, z)$  space rather than using the method proposed in section 5, where a representative time series is created for only regions with ongoing convection prior to filtering and then subsequently filtered for the intraseasonal band. This distinction is important. By first intraseasonally

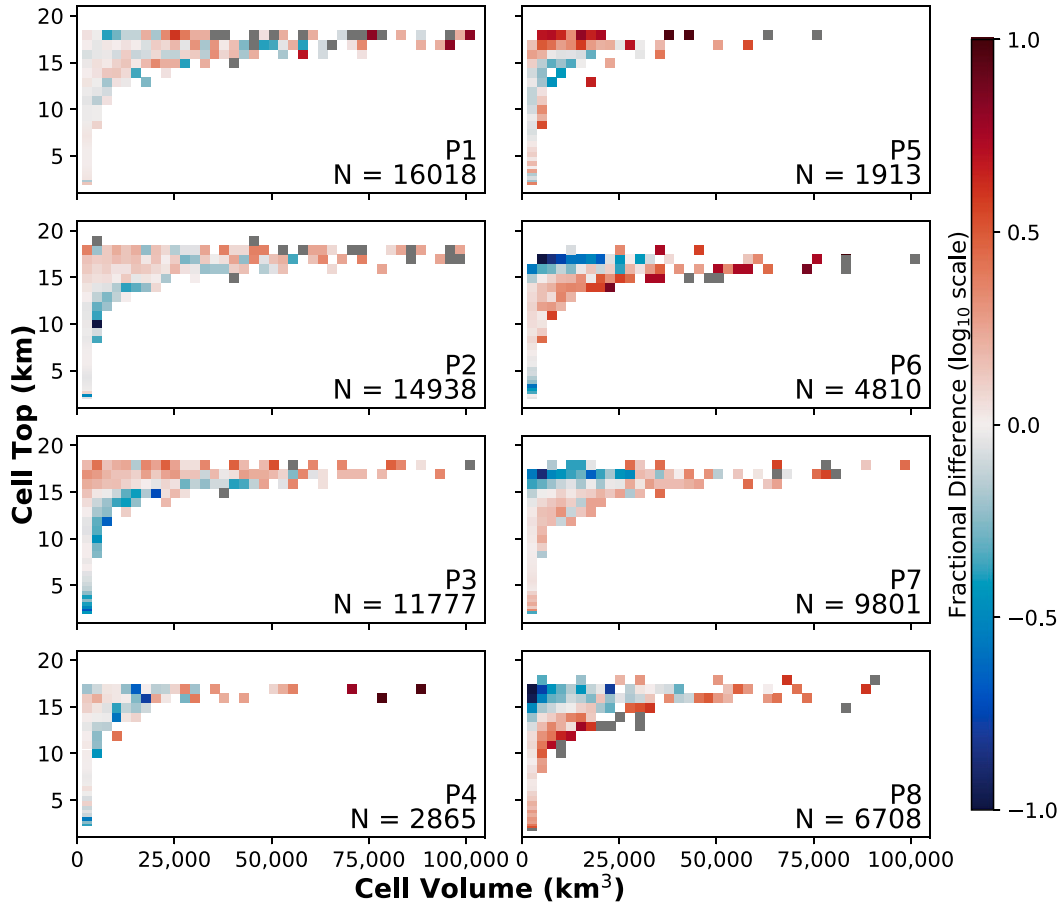


FIG. 11. As in Fig. 10, but for the convectively suppressed region of the MJO.

filtering the atmospheric state variables separately for each  $(x, y, z)$  location, we ensure that high-frequency impacts of convection on the atmospheric state are removed and only intraseasonal variability is retained. But, if a singular time series were generated that represented the atmospheric state at convective initiation and then subsequently filtered for the intraseasonal band, this time series would be selectively contaminated by high-frequency variability associated with convection and thereby not representative of intraseasonal anomalies associated with the regional character of the MJO. Therefore, after careful consideration we first filter each  $(x, y, z)$  location for the intraseasonal time scales prior to sampling from the regions in which convection occurs.

Vertical wind shear anomalies were then calculated via a second-order finite difference approximation to the vertical gradient in the low-frequency wind anomalies for the zonal and meridional wind components. Surface-based CAPE and CIN anomalies were calculated according to a more complicated procedure. The base-state CAPE and CIN were first calculated from

the mean temperature and water vapor mixing ratio profiles throughout the entire duration of the simulation for each grid point. Then, the low-frequency anomalies in temperature and water vapor mixing ratio for each  $(x, y, z)$  grid cell were added to the simulation-mean temperature and water vapor mixing ratio profiles, and the CAPE and CIN values for these perturbed profiles were calculated. The low-frequency CAPE and CIN anomalies were then estimated to be the difference between the CAPE and CIN values for the perturbed profiles and the base-state, simulation mean profiles. This procedure rendered anomalous vertical wind shear, CAPE, and CIN profiles at each location in  $(x, y)$  space for all time steps within the simulation.

Figure 12 shows the intraseasonal anomalies in various wind shear parameters, CAPE, and CIN at convective initiation throughout the simulation, within the convectively enhanced region of the MJO as defined by OMI. The total wind shear is defined as the shear of the wind magnitude, and the wind magnitude is calculated before taking the vertical gradient. Note that

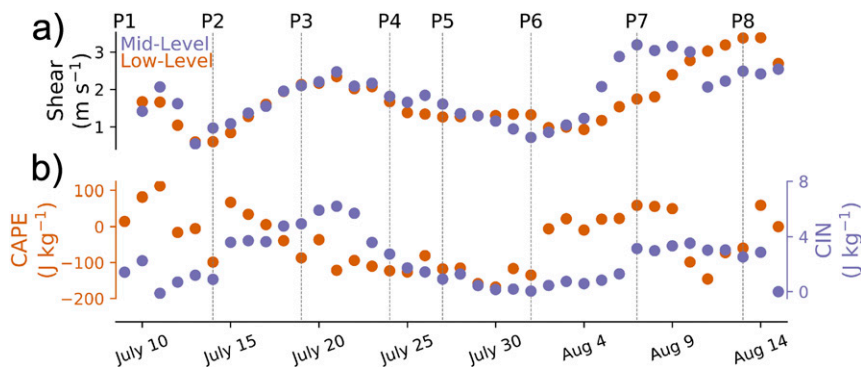


FIG. 12. Low-frequency ( $>20$  days) anomalies in the atmospheric state at convective initiation within the convectively enhanced lobe of the boreal summer MJO for (a) low- and midlevel shear and (b) CAPE and CIN. Low- and midlevel shear are defined as the shear magnitude from 1000 to 800 hPa and 800 to 400 hPa, respectively. The anomalies are composited by day. Refer to section 6 for further details regarding how these values are calculated.

Fig. 12a defines low-level vertical wind shear as the magnitude of the difference between the 1000- and 800-hPa wind vectors and the midlevel vertical wind shear as the difference between the 800- and 400-hPa wind vectors. These pressure levels are as defined by LeMone et al. (1998), which found a robust relationship between these definitions of low- and midlevel shear, CAPE, and CIN, and convective evolution within the tropics. While the climatological values of shear and bulk tropospheric instability may change across the domain depending on orography and latitude, this analysis considers intraseasonal anomalies from the simulation mean and therefore ignores any higher-frequency geographical dependences of the climatologies of these quantities. For example, the intraseasonal filtering removes impacts of the diurnal cycle, or any other mode of variability with periods of less than 20 days. It is worth noting that the climatological upper-tropospheric winds are easterly and lower-tropospheric winds are westerly across the entire domain (not shown).

The evolution of the atmospheric state at convective initiation may partially explain the relationships between convective morphology and the MJO presented in section 5. As a reminder, the intraseasonal time scale of convective morphology within the convectively enhanced portion of the dipole proceeds as follows: increased cell longevity in the initial phases, followed by increased cell number in the intermediate phases, progressing into increased cell volume in the terminal phases (Fig. 9a). Within the tropics, atmospheric thermodynamics govern convective longevity and depth, while kinematics govern cell structure (LeMone et al. 1998). For a uniform background environment, decreased low- and midlevel shear encourages isolated

convective elements, while a relative increase in either low- or midlevel shear encourages upscale growth (LeMone et al. 1998). The anomalously expansive convection that occurs during the latter phases of the MJO is therefore likely supported by the relative increase in both low- and midlevel shear during these phases (Fig. 12a). It is also possible that the relative reduction in low- and midlevel shear during phases 4–6 supports the greater number of convective cells during these intermediate phases, although this relationship is somewhat muddled by the increase in wind shear during phase 3.

The relationship between the evolution of the atmospheric thermodynamic state and convective organization is more robust. Generally, an increase in mid- to upper-level moisture supports longer-lasting convection, and reduced stability encourages deeper convective cells that repopulate more readily through cold pool interactions, as suggested by Barnes and Houze (2013) and LeMone et al. (1998). The increased instability in the latter phases of the MJO may support the deeper convective cells depicted in Fig. 10, although during the intermediate phases the change in stability is more complicated, as both CAPE and CIN decrease. It seems that an increase in low- to midtropospheric moisture in the early and late phases of the MJO is predominantly responsible for the increased cell longevity during these phases (Fig. 13). The increased longevity supported by the anomalously high values of low- to midtropospheric moisture content may be related to the increased cell volume during these periods. Should convective cells be maintained for a longer period of time, there is an increased likelihood that the cells can interact with surrounding convective elements and grow upscale. It is also possible that as cells grow in expanse, they become more immune to entrainment of ambient dry air, and can

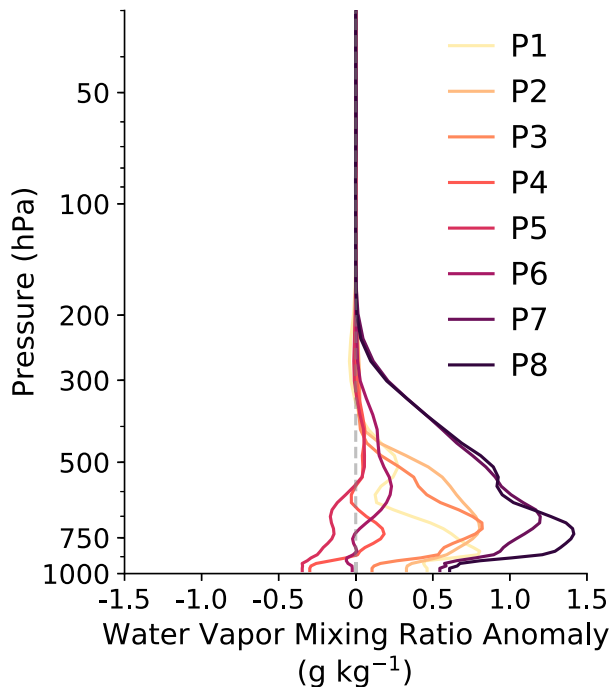


FIG. 13. Intraseasonal (>20 days) anomalies in water vapor mixing ratio at convective initiation within the convectively enhanced lobe of the MJO for each MJO phase. Refer to section 6 for further details regarding how these values are calculated.

therefore persist for a longer period of time. From a broader perspective, the relationship between the bulk thermodynamic and kinematic characteristics of the atmosphere seem to best explain the evolution of convective cell volume and longevity, but do not seem to be strongly tied to the number of cells.

## 7. Summary and conclusions

The MJO exhibits pronounced multiscale structure, spanning from regional convective anomalies with scales of thousands of kilometers to mesoscale convective features that are best defined by their individual convective updrafts. A plethora of research questions remain unanswered regarding the importance of spatial and temporal scales within the MJO, including how the regional intraseasonal anomalies and individual convective features interact. CRMs offer a unique opportunity to capture much of the breadth of scales within the MJO, as they permit the development of cloud structures and therefore the direct interpretation of interactions between the meso- and regional-scale structures of the MJO. We therefore used a CRM to investigate the relationship between convective cell morphology and regional anomalies associated with the MJO.

A boreal summer MJO event was simulated, which spanned from 10 July through 17 August 2016 and persisted throughout the entire MJO phase space as a strong convective anomaly (Fig. 2). The simulation domain was centered over the Maritime Continent and South China Sea, since these regions experience the peak intensity of convective anomalies throughout the MJO life cycle (Figs. 1 and 3). The lateral boundaries of the simulation were constrained by ERA5, while the interior of the domain was allowed to freely evolve according to the physics of the CRM. This ensured that while the synoptic- and regional-scale structure of the MJO was maintained by ERA5 through the lateral boundary conditions, the mesoscale identity of the MJO was captured directly by the CRM. In doing so, we permitted the direct investigation of how deep convective structures interact with the regional convective anomalies associated with the MJO.

The implications of this work are most focused on the evolution of the boreal summer MJO over the chosen simulation domain, which encompasses a majority of the Maritime Continent. There are, however, possibilities that the relationship discovered is exclusive to the simulation domain, and may change farther east toward the tropical Pacific or west within the Indian Ocean. We focus on the Maritime Continent since the evolution of the MJO is particularly complicated over this region, although it would be meritorious to repeat the presented simulation over different domains of the Indo-Pacific region. With that said, our results do broadly suggest that the mesoscales and intraseasonal scales of the MJO are closely related, and that the mesoscales undergo a distinct series of transitions as the MJO passes over the core of the Maritime Continent.

The convective population was sampled using a convective cloud tracking algorithm and then analyzed for its relationship with the intraseasonal character of the MJO. We focus on the convective aspects of the MJO because of the different microphysical and thermodynamic processes that govern the evolution of convective and stratiform precipitation (Houze 1997), although completing an analysis for solely stratiform precipitation would be a worthwhile endeavor as well. Using the convective cloud tracking algorithm, approximately 180 000 convective cells were identified throughout the simulation, whereby a convective cell was defined as a contiguous expanse of convectively generated cloud that was actively precipitating. We considered the evolution of the convective populations within the MJO convective anomalies according to three characteristics: the number of convective cells, convective cell volume, and convective cell longevity. Time series of these three variables were generated for

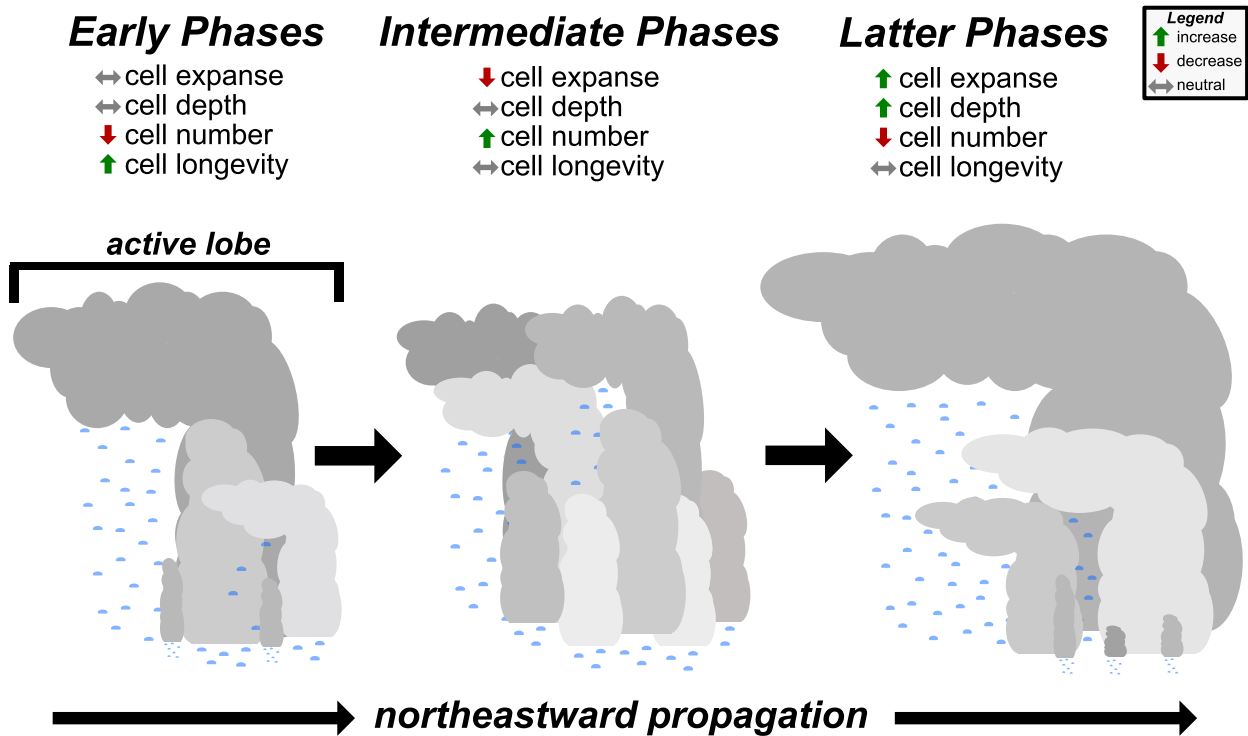


FIG. 14. Schematic depicting the intraseasonal character of convective morphology within the convectively active region of the MJO. This schematic summarizes the findings detailed in section 5. The raindrops do not have physical meaning aside from indicating that only precipitating convective clouds were included within the analysis.

both the convectively enhanced and suppressed lobes of the MJO, and filtered to include only variability with periods greater than 20 days. In doing so, the relationship between convective morphology and intraseasonal variability, and therefore likely the MJO, was isolated. We do not separate the analysis by land and ocean, since we feel it artificial to distinguish between the two given that the boreal summer MJO convective envelope is broad and captures both land and ocean points. Convective morphology changes induced by interactions with land are likely important for BSISO maintenance and propagation, however, and this would therefore be an interesting avenue for future research.

We found that a pronounced progressive relationship in convective morphology occurs within the convectively enhanced lobe of the MJO across the Maritime Continent, as follows: increased cell longevity in the initial phases, followed by increased cell number in the intermediate phases, progressing into increased cell volume in the terminal phases (Fig. 9a). Furthermore, the depth of convective cells tends to be greatest during the latter phases of the MJO (Fig. 10). This evolution is depicted schematically in Fig. 14. The cell morphology is less variable within the convectively suppressed lobe of the MJO, wherein the population of convective cells

generally maintains a singular identity throughout the entire life cycle of the MJO. These relationships are apparent within both spectrally filtered time series of convective number, volume, and longevity, and within two-dimensional histograms composited by MJO phase.

By filtering for intraseasonal time scales, these relationships are not separable from the impacts of geography on intraseasonal variability within the Maritime Continent, but are separable from higher-frequency modes of variability tied to geography such as the diurnal cycle. However, the similarities between the phase composited histograms and the spectral analysis suggests that the relationship within the spectrally filtered time series is not disrupted by higher-frequency modes of variability. Particularly, this relative lack of importance of the higher-frequency modes suggests that if geographic variability is important to the relationship between mesoscale convection and the intraseasonal time scales of the MJO, the importance is well captured by the intraseasonal relationship.

The relationship between the progressive morphology of the convective population and the low-frequency atmospheric response to the MJO is complicated. Bulk atmospheric characteristics such as vertical wind shear and CAPE have previously been used to separate environments most conducive for varying types of convective

morphology. For example, increased vertical wind shear is favorable for upscale growth, while reduced vertical wind shear and increased convective instability favors a greater number of convective cells (LeMone et al. 1998). We therefore investigated whether intraseasonal anomalies in wind shear and convective instability dictate the progressive convective morphology within the convectively enhanced lobe of the MJO. In essence, the evolution of intraseasonal anomalies in water vapor mixing ratio seem to most influence convective cell volume and longevity, whereas the number of convective cells appears to be tied to another source of variability not identified within this study. The predominant influence of water vapor is consistent with an extensive body of literature on the modulation of convection by the MJO via low-frequency variability in atmospheric water vapor (e.g., Adames and Kim 2016; Raymond and Fuchs 2009; Sobel and Maloney 2013).

The intraseasonal relationship between the MJO and the evolution of convective cells within its enhanced and suppressed regions across the Maritime Continent may have broader implications for the large-scale structure and evolution for the MJO. For example, the distribution of cloud within the dipole of the MJO is related to the redistribution of water vapor from the boundary layer into the free troposphere, which has been found to be an important factor in the overall evolution of the MJO and other convectively coupled equatorial waves (Peters and Bretherton 2006; Benedict and Randall 2007; Adames and Kim 2016). It would therefore be interesting to expand upon the existing literature citing the importance of convective features in the upscale redistribution of water vapor using methods such as spectral flux, as detailed in Arbic et al. (2012) and Hayashi (1980), to identify the scales most important for driving the aggregation of water vapor anomalies. Another interesting avenue for future research could be to expand or shift the simulation domain to test whether a similar relationship holds across the rest of the Indo-Pacific region.

Additional upscale influences may arise from cloud-radiative feedbacks, since changes in the distribution of cloud have been shown to impact the propagation and intensity of the intraseasonal structure of the MJO (Flatau et al. 1997; Arnold and Randall 2015; Kim et al. 2015; Wolding et al. 2016; Adames and Kim 2016). While not directly investigated within this study, it is plausible that the aggregation of mesoscale convective clouds with different morphologies could impact the radiative feedbacks of clouds onto the larger-scale structure of the MJO when integrated across space and time. Regardless of the direction of influence that causes the relationship, this work is generally supportive of the idea that the mesoscales and intraseasonal scales are closely related within the tropics.

*Acknowledgments.* Benjamin A. Toms was funded in part by Office of Naval Research Grant N00014-16-1-3093 and was otherwise supported by the U.S. Department of Energy Computational Science Graduate Fellowship via Grant DE-FG02-97ER25308. Susan C. van den Heever was funded by Office of Naval Research Grant N00014-16-1-3093. Stephen M. Saleeby was funded by National Aeronautics and Space Administration Grant 80NSSC18KD149. Emily M. Riley Dellaripa and Eric D. Maloney were funded by Office of Naval Research Grant N00014-16 and National Aeronautics and Space Administration Grant NNX17AH77G. We thank the reviewers, Mitch Moncrieff and two who remained anonymous, for their comments, which improved the manuscript.

## REFERENCES

- Adames, A. F., and D. Kim, 2016: The MJO as a dispersive, convectively coupled moisture wave: Theory and observations. *J. Atmos. Sci.*, **73**, 913–941, <https://doi.org/10.1175/JAS-D-15-0170.1>.
- Arbic, B. K., R. B. Scott, G. R. Flierl, A. J. Morten, J. G. Richman, and J. F. Shriver, 2012: Nonlinear cascades of surface oceanic geostrophic kinetic energy in the frequency domain. *J. Phys. Oceanogr.*, **42**, 1577–1600, <https://doi.org/10.1175/JPO-D-11-0151.1>.
- Arnold, N. P., and D. A. Randall, 2015: Global-scale convective aggregation: Implications for the Madden–Julian oscillation. *J. Adv. Model. Earth Syst.*, **7**, 1499–1518, <https://doi.org/10.1002/2015MS000498>.
- Barnes, H. C., and R. A. Houze Jr., 2013: The precipitating cloud population of the Madden–Julian oscillation over the Indian and west Pacific Oceans. *J. Geophys. Res. Atmos.*, **118**, 6996–7023, <https://doi.org/10.1002/jgrd.50375>.
- Benedict, J. J., and D. A. Randall, 2007: Observed characteristics of the MJO relative to maximum rainfall. *J. Atmos. Sci.*, **64**, 2332–2354, <https://doi.org/10.1175/JAS3968.1>.
- Biasutti, M., S. E. Yuter, C. D. Burleyson, and A. H. Sobel, 2012: Very high resolution rainfall patterns measured by TRMM Precipitation Radar: Seasonal and diurnal cycles. *Climate Dyn.*, **39**, 239–258, <https://doi.org/10.1007/s00382-011-1146-6>.
- Chang, E. K., 1995: The influence of Hadley circulation intensity changes on extratropical climate in an idealized model. *J. Atmos. Sci.*, **52**, 2006–2024, [https://doi.org/10.1175/1520-0469\(1995\)052<2006:TIOHCI>2.0.CO;2](https://doi.org/10.1175/1520-0469(1995)052<2006:TIOHCI>2.0.CO;2).
- Copernicus Climate Change Service, 2017: ERA5: Fifth generation of ECMWF atmospheric reanalysis of the global climate. Copernicus Climate Change Service, accessed December 2017, <https://climate.copernicus.eu/>.
- Cotton, W. R., and Coauthors, 2003: RAMS 2001: Current status and future directions. *Meteor. Atmos. Phys.*, **82**, 5–29, <https://doi.org/10.1007/s00703-001-0584-9>.
- DeMott, P. J., and Coauthors, 2010: Predicting global atmospheric ice nuclei distributions and their impacts on climate. *Proc. Natl. Acad. Sci.*, **107**, 11 217–11 222, <https://doi.org/10.1073/pnas.0910818107>.
- Dias, J., S. N. Tulich, and G. N. Kiladis, 2012: An object-based approach to assessing the organization of tropical convection. *J. Atmos. Sci.*, **69**, 2488–2504, <https://doi.org/10.1175/JAS-D-11-0293.1>.
- Fierro, A. O., J. Simpson, M. A. LeMone, J. M. Straka, and B. F. Smull, 2009: On how hot towers fuel the Hadley cell: An

- observational and modeling study of line-organized convection in the equatorial trough from TOGA COARE. *J. Atmos. Sci.*, **66**, 2730–2746, <https://doi.org/10.1175/2009JAS3017.1>.
- Flatau, M., P. J. Flatau, P. Phoebus, and P. P. Niiler, 1997: The feedback between equatorial convection and local radiative and evaporative processes: The implications for intraseasonal oscillations. *J. Atmos. Sci.*, **54**, 2373–2386, [https://doi.org/10.1175/1520-0469\(1997\)054<2373:TFBECA>2.0.CO;2](https://doi.org/10.1175/1520-0469(1997)054<2373:TFBECA>2.0.CO;2).
- Harrington, J. Y., 1997: The effects of radiative and microphysical processes on simulated warm and transition season Arctic stratus. Ph.D. dissertation, Colorado State University, 289 pp.
- Hayashi, Y., 1980: Estimation of nonlinear energy transfer spectra by the cross-spectral method. *J. Atmos. Sci.*, **37**, 299–307, [https://doi.org/10.1175/1520-0469\(1980\)037<0299:EONETS>2.0.CO;2](https://doi.org/10.1175/1520-0469(1980)037<0299:EONETS>2.0.CO;2).
- Hendon, H. H., and B. Liebmann, 1991: The structure and annual variation of antisymmetric fluctuations of tropical convection and their association with Rossby–gravity waves. *J. Atmos. Sci.*, **48**, 2127–2140, [https://doi.org/10.1175/1520-0469\(1991\)048<2127:TSAAVO>2.0.CO;2](https://doi.org/10.1175/1520-0469(1991)048<2127:TSAAVO>2.0.CO;2).
- , and —, 1994: Organization of convection within the Madden–Julian oscillation. *J. Geophys. Res.*, **99**, 8073–8083, <https://doi.org/10.1029/94JD00045>.
- , and M. L. Salby, 1994: The life cycle of the Madden–Julian oscillation. *J. Atmos. Sci.*, **51**, 2225–2237, [https://doi.org/10.1175/1520-0469\(1994\)051<2225:TLCOTM>2.0.CO;2](https://doi.org/10.1175/1520-0469(1994)051<2225:TLCOTM>2.0.CO;2).
- Hou, A. Y., and Coauthors, 2014: The Global Precipitation Measurement mission. *Bull. Amer. Meteor. Soc.*, **95**, 701–722, <https://doi.org/10.1175/BAMS-D-13-00164.1>.
- Houze, R. A., Jr., 1997: Stratiform precipitation in regions of convection: A meteorological paradox? *Bull. Amer. Meteor. Soc.*, **78**, 2179–2196, [https://doi.org/10.1175/1520-0477\(1997\)078<2179:SPIROC>2.0.CO;2](https://doi.org/10.1175/1520-0477(1997)078<2179:SPIROC>2.0.CO;2).
- Hsu, H.-H., C.-H. Hung, A.-K. Lo, C.-C. Wu, and C.-W. Hung, 2008: Influence of tropical cyclones on the estimation of climate variability in the tropical western North Pacific. *J. Climate*, **21**, 2960–2975, <https://doi.org/10.1175/2007JCLI1847.1>.
- Huffman, G. J., D. T. Bolvin, D. Braithwaite, K. Hsu, R. Joyce, P. Xie, and S.-H. Yoo, 2015: NASA Global Precipitation Measurement (GPM) integrated Multi-Satellite Retrievals for GPM (IMERG). Algorithm Theoretical Basis Doc., version 4, 28 pp.
- Jiang, X., and Coauthors, 2015: Vertical structure and physical processes of the Madden–Julian oscillation: Exploring key model physics in climate simulations. *J. Geophys. Res. Atmos.*, **120**, 4718–4748, <https://doi.org/10.1002/2014JD022375>.
- , A. F. Adames, M. Zhao, D. Waliser, and E. Maloney, 2018: A unified moisture mode framework for seasonality of the Madden–Julian oscillation. *J. Climate*, **31**, 4215–4224, <https://doi.org/10.1175/JCLI-D-17-0671.1>.
- Johnson, R. H., and D. C. Kriete, 1982: Thermodynamic and circulation characteristics, of winter monsoon tropical mesoscale convection. *Mon. Wea. Rev.*, **110**, 1898–1911, [https://doi.org/10.1175/1520-0493\(1982\)110<1898:TACCOW>2.0.CO;2](https://doi.org/10.1175/1520-0493(1982)110<1898:TACCOW>2.0.CO;2).
- Kikuchi, K., and B. Wang, 2010: Formation of tropical cyclones in the northern Indian Ocean associated with two types of tropical intraseasonal oscillation modes. *J. Meteor. Soc. Japan*, **88**, 475–496, <https://doi.org/10.2151/jmsj.2010-313>.
- , —, and Y. Kajikawa, 2012: Bimodal representation of the tropical intraseasonal oscillation. *Climate Dyn.*, **38**, 1989–2000, <https://doi.org/10.1007/s00382-011-1159-1>.
- , G. N. Kiladis, J. Dias, and T. Nasuno, 2018: Convectively coupled equatorial waves within the MJO during CINDY/DYNAMO: Slow Kelvin waves as building blocks. *Climate Dyn.*, **50**, 4211–4230, <https://doi.org/10.1007/s00382-017-3869-5>.
- Kiladis, G. N., and K. M. Weickmann, 1992: Circulation anomalies associated with tropical convection during northern winter. *Mon. Wea. Rev.*, **120**, 1900–1923, [https://doi.org/10.1175/1520-0493\(1992\)120<1900:CAAWTC>2.0.CO;2](https://doi.org/10.1175/1520-0493(1992)120<1900:CAAWTC>2.0.CO;2).
- , K. H. Straub, and P. T. Haertel, 2005: Zonal and vertical structure of the Madden–Julian oscillation. *J. Atmos. Sci.*, **62**, 2790–2809, <https://doi.org/10.1175/JAS3520.1>.
- , J. Dias, K. H. Straub, M. C. Wheeler, S. N. Tulich, K. Kikuchi, K. M. Weickmann, and M. J. Ventrice, 2014: A comparison of OLR and circulation-based indices for tracking the MJO. *Mon. Wea. Rev.*, **142**, 1697–1715, <https://doi.org/10.1175/MWR-D-13-00301.1>.
- Kim, D., M.-S. Ahn, I.-S. Kang, and A. D. Del Genio, 2015: Role of longwave cloud–radiation feedback in the simulation of the Madden–Julian oscillation. *J. Climate*, **28**, 6979–6994, <https://doi.org/10.1175/JCLI-D-14-00767.1>.
- Klemp, J. B., and R. B. Wilhelmson, 1978: The simulation of three-dimensional convective storm dynamics. *J. Atmos. Sci.*, **35**, 1070–1096, [https://doi.org/10.1175/1520-0469\(1978\)035<1070:TSOTDC>2.0.CO;2](https://doi.org/10.1175/1520-0469(1978)035<1070:TSOTDC>2.0.CO;2).
- Lafore, J.-P., and M. W. Moncrieff, 1989: A numerical investigation of the organization and interaction of the convective and stratiform regions of tropical squall lines. *J. Atmos. Sci.*, **46**, 521–544, [https://doi.org/10.1175/1520-0469\(1989\)046<0521:ANIOTO>2.0.CO;2](https://doi.org/10.1175/1520-0469(1989)046<0521:ANIOTO>2.0.CO;2).
- Lane, T. P., M. J. Reeder, and T. L. Clark, 2001: Numerical modeling of gravity wave generation by deep tropical convection. *J. Atmos. Sci.*, **58**, 1249–1274, [https://doi.org/10.1175/1520-0469\(2001\)058<1249:NMOGWG>2.0.CO;2](https://doi.org/10.1175/1520-0469(2001)058<1249:NMOGWG>2.0.CO;2).
- LeMone, M. A., E. J. Zipser, and S. B. Trier, 1998: The role of environmental shear and thermodynamic conditions in determining the structure and evolution of mesoscale convective systems during TOGA COARE. *J. Atmos. Sci.*, **55**, 3493–3518, [https://doi.org/10.1175/1520-0469\(1998\)055<3493:TROESA>2.0.CO;2](https://doi.org/10.1175/1520-0469(1998)055<3493:TROESA>2.0.CO;2).
- Li, R. C., and W. Zhou, 2013: Modulation of western North Pacific tropical cyclone activity by the ISO. Part I: Genesis and intensity. *J. Climate*, **26**, 2904–2918, <https://doi.org/10.1175/JCLI-D-12-00210.1>.
- Liebmann, B., and C. A. Smith, 1996: Description of a complete (interpolated) outgoing longwave radiation dataset. *Bull. Amer. Meteor. Soc.*, **77**, 1275–1277, <https://doi.org/10.1175/1520-0477-77.6.1274>.
- Lorenz, E. N., 1969: The nature of the global circulation of the atmosphere: A present view. *The Global Circulation of the Atmosphere*, Royal Meteorological Society, 3–23.
- Love, B. S., A. J. Matthews, and G. M. Lister, 2011: The diurnal cycle of precipitation over the Maritime Continent in a high-resolution atmospheric model. *Quart. J. Roy. Meteor. Soc.*, **137**, 934–947, <https://doi.org/10.1002/qj.809>.
- Madden, R. A., 1986: Seasonal variations of the 40–50 day oscillation in the tropics. *J. Atmos. Sci.*, **43**, 3138–3158, [https://doi.org/10.1175/1520-0469\(1986\)043<3138:SVOTDO>2.0.CO;2](https://doi.org/10.1175/1520-0469(1986)043<3138:SVOTDO>2.0.CO;2).
- , and P. R. Julian, 1971: Detection of a 40–50 day oscillation in the zonal wind in the tropical Pacific. *J. Atmos. Sci.*, **28**, 702–708, [https://doi.org/10.1175/1520-0469\(1971\)028<0702:DOADOI>2.0.CO;2](https://doi.org/10.1175/1520-0469(1971)028<0702:DOADOI>2.0.CO;2).
- , and —, 1972: Description of global-scale circulation cells in the tropics with a 40–50 day period. *J. Atmos. Sci.*, **29**, 1109–1123, [https://doi.org/10.1175/1520-0469\(1972\)029<1109:DOGSCC>2.0.CO;2](https://doi.org/10.1175/1520-0469(1972)029<1109:DOGSCC>2.0.CO;2).
- , and —, 1994: Observations of the 40–50-day tropical oscillation—A review. *Mon. Wea. Rev.*, **122**, 814–837, [https://doi.org/10.1175/1520-0493\(1994\)122<0814:OOTDTCO>2.0.CO;2](https://doi.org/10.1175/1520-0493(1994)122<0814:OOTDTCO>2.0.CO;2).

- Maloney, E. D., and M. J. Dickinson, 2003: The intraseasonal oscillation and the energetics of summertime tropical western North Pacific synoptic-scale disturbances. *J. Atmos. Sci.*, **60**, 2153–2168, [https://doi.org/10.1175/1520-0469\(2003\)060<2153:TIOATE>2.0.CO;2](https://doi.org/10.1175/1520-0469(2003)060<2153:TIOATE>2.0.CO;2).
- Mapes, B., S. Tulich, J. Lin, and P. Zuidema, 2006: The meso-scale convection life cycle: Building block or prototype for large-scale tropical waves? *Dyn. Atmos. Oceans*, **42**, 3–29, <https://doi.org/10.1016/j.dynatmoce.2006.03.003>.
- Meyers, M. P., R. L. Walko, J. Y. Harrington, and W. R. Cotton, 1997: New RAMS cloud microphysics parameterization. Part II: The two-moment scheme. *Atmos. Res.*, **45**, 3–39, [https://doi.org/10.1016/S0169-8095\(97\)00018-5](https://doi.org/10.1016/S0169-8095(97)00018-5).
- Moncrieff, M. W., 2010: The multiscale organization of moist convection and the intersection of weather and climate. *Climate Dynamics: Why Does Climate Vary?* *Geophys. Monogr.*, Vol. 189, Amer. Geophys. Union, 3–26, <https://doi.org/10.1029/2008GM000838>.
- , D. E. Waliser, M. J. Miller, M. A. Shapiro, G. R. Asrar, and J. Caughey, 2012: Multiscale convective organization and the YOTC virtual global field campaign. *Bull. Amer. Meteor. Soc.*, **93**, 1171–1187, <https://doi.org/10.1175/BAMS-D-11-00233.1>.
- , C. Liu, and P. Bogenschutz, 2017: Simulation, modeling, and dynamically based parameterization of organized tropical convection for global climate models. *J. Atmos. Sci.*, **74**, 1363–1380, <https://doi.org/10.1175/JAS-D-16-0166.1>.
- Peters, M. E., and C. S. Bretherton, 2006: Structure of tropical variability from a vertical mode perspective. *Theor. Comput. Fluid Dyn.*, **20**, 501–524, <https://doi.org/10.1007/s00162-006-0034-x>.
- Petersen, W. A., and S. A. Rutledge, 2001: Regional variability in tropical convection: Observations from TRMM. *J. Climate*, **14**, 3566–3586, [https://doi.org/10.1175/1520-0442\(2001\)014<3566:RVITCO>2.0.CO;2](https://doi.org/10.1175/1520-0442(2001)014<3566:RVITCO>2.0.CO;2).
- Raymond, D. J., and Z. Fuchs, 2009: Moisture modes and the Madden–Julian oscillation. *J. Climate*, **22**, 3031–3046, <https://doi.org/10.1175/2008JCLI2739.1>.
- Reynolds, R. W., N. A. Rayner, T. M. Smith, D. C. Stokes, and W. Wang, 2002: An improved in situ and satellite SST analysis for climate. *J. Climate*, **15**, 1609–1625, [https://doi.org/10.1175/1520-0442\(2002\)015<1609:AISAS>2.0.CO;2](https://doi.org/10.1175/1520-0442(2002)015<1609:AISAS>2.0.CO;2).
- Riehl, H., and J. S. Malkus, 1957: On the heat balance and maintenance of circulation in the trades. *Quart. J. Roy. Meteor. Soc.*, **83**, 21–29, <https://doi.org/10.1002/qj.49708335503>.
- Riley, E. M., B. E. Mapes, and S. N. Tulich, 2011: Clouds associated with the Madden–Julian oscillation: A new perspective from *CloudSat*. *J. Atmos. Sci.*, **68**, 3032–3051, <https://doi.org/10.1175/JAS-D-11-030.1>.
- , E. Maloney, and S. C. van den Heever, 2018: Wind–flux feedbacks and convective organization during the November 2011 MJO event in a high-resolution model. *J. Atmos. Sci.*, **75**, 57–84, <https://doi.org/10.1175/JAS-D-16-0346.1>.
- Saleeby, S. M., and W. R. Cotton, 2004: A large-droplet mode and prognostic number concentration of cloud droplets in the Colorado State University Regional Atmospheric Modeling System (RAMS). Part I: Module descriptions and supercell test simulations. *J. Appl. Meteor.*, **43**, 182–195, [https://doi.org/10.1175/1520-0450\(2004\)043<0182:ALMAPN>2.0.CO;2](https://doi.org/10.1175/1520-0450(2004)043<0182:ALMAPN>2.0.CO;2).
- , and S. C. van den Heever, 2013: Developments in the CSU–RAMS aerosol model: Emissions, nucleation, regeneration, deposition, and radiation. *J. Appl. Meteor. Climatol.*, **52**, 2601–2622, <https://doi.org/10.1175/JAMC-D-12-0312.1>.
- Smagorinsky, J., 1963: General circulation experiments with the primitive equations: I. The basic experiment. *Mon. Wea. Rev.*, **91**, 99–164, [https://doi.org/10.1175/1520-0493\(1963\)091<0099:GCEWTP>2.3.CO;2](https://doi.org/10.1175/1520-0493(1963)091<0099:GCEWTP>2.3.CO;2).
- Sobel, A., and E. Maloney, 2013: Moisture modes and the eastward propagation of the MJO. *J. Atmos. Sci.*, **70**, 187–192, <https://doi.org/10.1175/JAS-D-12-0189.1>.
- Vincent, C. L., and T. P. Lane, 2018: Mesoscale variation in diabatic heating around Sumatra, and its modulation with the Madden–Julian oscillation. *Mon. Wea. Rev.*, **146**, 2599–2614, <https://doi.org/10.1175/MWR-D-17-0392.1>.
- Waliser, D. E., R. Murtugudde, and L. E. Lucas, 2004: Indo-Pacific Ocean response to atmospheric intraseasonal variability: 2. Boreal summer and the intraseasonal oscillation. *J. Geophys. Res.*, **109**, C03030, <https://doi.org/10.1029/2003JC002002>.
- Wang, B., 2002: Rainy season of the Asian–Pacific summer monsoon. *J. Climate*, **15**, 386–398, [https://doi.org/10.1175/1520-0442\(2002\)015<0386:RSOTAP>2.0.CO;2](https://doi.org/10.1175/1520-0442(2002)015<0386:RSOTAP>2.0.CO;2).
- , and X. Xie, 1997: A model for the boreal summer intraseasonal oscillation. *J. Atmos. Sci.*, **54**, 72–86, [https://doi.org/10.1175/1520-0469\(1997\)054<0072:AMFTBS>2.0.CO;2](https://doi.org/10.1175/1520-0469(1997)054<0072:AMFTBS>2.0.CO;2).
- Wheeler, M. C., and H. H. Hendon, 2004: An all-season real-time multivariate MJO index: Development of an index for monitoring and prediction. *Mon. Wea. Rev.*, **132**, 1917–1932, [https://doi.org/10.1175/1520-0493\(2004\)132<1917:AARMMI>2.0.CO;2](https://doi.org/10.1175/1520-0493(2004)132<1917:AARMMI>2.0.CO;2).
- Wolding, B. O., E. D. Maloney, and M. Branson, 2016: Vertically resolved weak temperature gradient analysis of the Madden–Julian oscillation in SP-CESM. *J. Adv. Model. Earth Syst.*, **8**, 1586–1619, <https://doi.org/10.1002/2016MS000724>.
- Wu, M.-L. C., S. D. Schubert, M. J. Suarez, P. J. Pegion, and D. E. Waliser, 2006: Seasonality and meridional propagation of the MJO. *J. Climate*, **19**, 1901–1921, <https://doi.org/10.1175/JCLI3680.1>.
- Xu, H., S.-P. Xie, Y. Wang, W. Zhuang, and D. Wang, 2008: Orographic effects on South China Sea summer climate. *Meteor. Atmos. Phys.*, **100**, 275–289, <https://doi.org/10.1007/s00703-008-0309-4>.
- Yang, D., and A. P. Ingersoll, 2011: Testing the hypothesis that the MJO is a mixed Rossby–gravity wave packet. *J. Atmos. Sci.*, **68**, 226–239, <https://doi.org/10.1175/2010JAS3563.1>.
- Yang, Q., A. J. Majda, and M. W. Moncrieff, 2019: Upscale impact of mesoscale convective systems and its parameterization in an idealized GCM for an MJO analog above the equator. *J. Atmos. Sci.*, **76**, 865–892, <https://doi.org/10.1175/JAS-D-18-0260.1>.
- Zhang, C., 2005: Madden–Julian oscillation. *Rev. Geophys.*, **43**, RG2003, <https://doi.org/10.1029/2004RG000158>.
- , and M. Dong, 2004: Seasonality in the Madden–Julian oscillation. *J. Climate*, **17**, 3169–3180, [https://doi.org/10.1175/1520-0442\(2004\)017<3169:SITMO>2.0.CO;2](https://doi.org/10.1175/1520-0442(2004)017<3169:SITMO>2.0.CO;2).
- Zhang, G. J., and M. Mu, 2005: Simulation of the Madden–Julian oscillation in the NCAR CCM3 using a revised Zhang–McFarlane convection parameterization scheme. *J. Climate*, **18**, 4046–4064, <https://doi.org/10.1175/JCLI3508.1>.
- Zhang, Y., T. Li, B. Wang, and G. Wu, 2002: Onset of the summer monsoon over the Indochina Peninsula: Climatology and interannual variations. *J. Climate*, **15**, 3206–3221, [https://doi.org/10.1175/1520-0442\(2002\)015<3206:OOTSMO>2.0.CO;2](https://doi.org/10.1175/1520-0442(2002)015<3206:OOTSMO>2.0.CO;2).
- Zuluaga, M. D., and R. A. Houze Jr., 2013: Evolution of the population of precipitating convective systems over the equatorial Indian Ocean in active phases of the Madden–Julian oscillation. *J. Atmos. Sci.*, **70**, 2713–2725, <https://doi.org/10.1175/JAS-D-12-0311.1>.